



* limbic system / Brodmann field?

Four distinct trajectories of tau deposition identified in Alzheimer's disease

Jacob W. Vogel  , Alexandra L. Young², Neil P. Oxtoby , Ruben Smith , Rik Ossenkoppele ,
Olof T. Strandberg⁵, Renaud La Joie , Leon M. Aksman , Michel J. Grothe ,
Yasser Iturria-Medina , the Alzheimer's Disease Neuroimaging Initiative*, Michael J. Pontecorvo ,
Michael D. Devous , Gil D. Rabinovici , Daniel C. Alexander , Chul Hyoung Lyoo ,
Alan C. Evans  and Oskar Hansson  

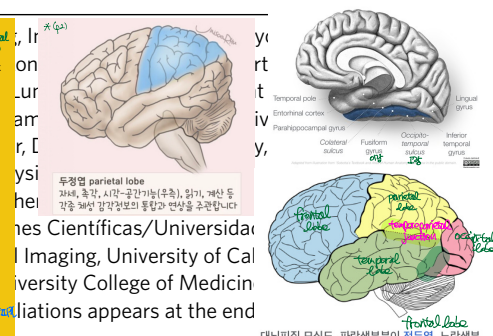
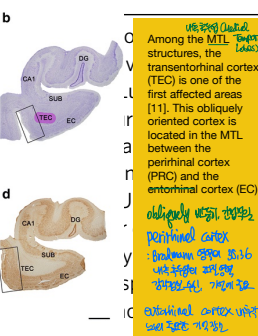
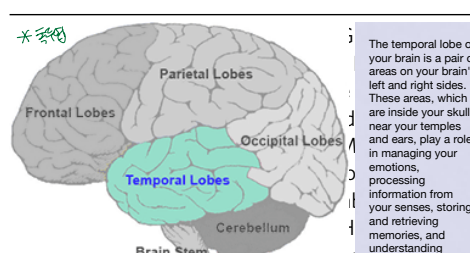
Alzheimer's disease (AD) is characterized by the spread of tau pathology throughout the cerebral cortex. This spreading pattern was thought to be fairly consistent across individuals, although recent work has demonstrated substantial variability in the population with AD. Using tau-positron emission tomography scans from 1,612 individuals, we identified 4 distinct spatiotemporal trajectories of tau pathology, ranging in prevalence from 18 to 33%. We replicated previously described limbic-predominant and medial temporal lobe-sparing patterns, while also discovering posterior and lateral temporal patterns resembling atypical clinical variants of AD. These 'subtypes' were stable during longitudinal follow-up and were replicated in a separate sample using a different radiotracer. The subtypes presented with distinct demographic and cognitive profiles and differing longitudinal outcomes. Additionally, network diffusion models implied that pathology originates and spreads through distinct corticolimbic networks in the different subtypes. Together, our results suggest that variation in tau pathology is common and systematic, perhaps warranting a re-examination of the notion of 'typical AD' and a revisiting of tau pathological staging.

AD is the leading cause of dementia worldwide and prevalence is expected to double in the next 20 years¹. At autopsy, AD presents with diffuse extracellular and neuritic amyloid- β ($A\beta$) plaques and intracellular neurofibrillary tangles and neuropil threads of hyperphosphorylated tau, along with extensive neurodegeneration^{2,3}. Leading hypotheses have postulated that these two hallmark proteins, $A\beta$ and tau, either alone or in combination, are causative agents in disease etiology and progression^{4,5}. Cortical tau colocalizes with cortical atrophy and predicts future neurodegeneration⁶, while the appearance of tau in specific cognitive networks leads to domain-specific cognitive impairments⁷. Recently, the focus of treatment discovery has shifted to tau and many therapeutic interventions are currently undergoing research and development. Therefore a better understanding of tau pathophysiology is of imminent need to aid the development of these interventions.

Tau tangles are thought to exhibit a stereotypical pattern of cortical spread, which has been formalized into the Braak staging system.^{8,9} The six Braak stages describe the first appearance of cortical tau tangles in the transentorhinal cortex, subsequent spread throughout the medial and basal temporal lobes, then into

neocortical associative regions and finally into the unimodal sensory and motor cortex⁹. While this stereotyped progression was derived from histopathological staining at autopsy, tau can now be measured in vivo in the human brain using positron emission tomography (PET). Early tau PET imaging studies described average spatial patterns that have mostly converged with the Braak staging system^{10,11}.

However, many examples have emerged of individual tau patterns that do not fit neatly into the Braak staging system. A medial temporal lobe (MTL)-sparing phenotype with extensive cortical tau burden but limited MTL burden has been described, as well as a limbic-predominant phenotype with most prominent tau pathology in the limbic and medial temporal cortex, which were each associated with specific patient profiles¹²⁻¹⁴. In addition, clinical variants of AD have been described that exhibit specific patterns of pathology that deviate from the Braak staging scheme¹⁵, for example, posterior cortical atrophy (PCA)¹⁶, logopenic primary progressive aphasia (PPA)¹⁷ and others¹⁸. These latter clinical variants of AD are relatively uncommon and most frequently associated with early-onset AD but represent another example of atypical tau patterning.





Taken together, the examples above suggest that, while the Braak staging system is a good description of tau spreading at the population level, it does not account for systematic variability at the individual level. Variation in tau patterning may be indicative of a distinct underlying neurobiology^{19,20}, which may affect treatment response. Different subtypes may also have distinct rates and profiles of cognitive decline^{21,22}, potentially affecting clinical trials. For these reasons, a systematic description of variation in AD pathological spread is needed. Previous studies have provided invaluable information toward this effort^{12,13,23–26} but carry certain limitations. Pathology studies, for example, are limited by spatial sampling and semiquantitation. Neuroimaging studies have overcome some of those limitations but often use nonspecific measurements and rely on methods designed to parse spatial rather than spatiotemporal variation.

Here we present a systematic characterization of heterogeneity in tau patterning in AD. We amassed the largest and most diverse sample of tau PET data to date ($n=2,324$), covering the full clinical spectrum from asymptomatic through mild cognitive impairment (MCI) to AD dementia, allowing unprecedented power to detect and characterize AD subtypes. We fitted these data using the Subtype and Stage Inference (SuStaIn) model, a paradigm-shifting algorithm that combines disease progression modeling with traditional clustering to achieve probabilistic spatiotemporal partitioning and classification²³. SuStaIn requires only cross-sectional datasets to automatically detect multiple spatiotemporal trajectories and provides probabilistic and quantitative information for individualized inference. We applied SuStaIn to our multi-cohort sample of tau PET data to discover systematic spatiotemporal variation in tau spreading. We validated the subtypes across different PET radiotracers and validated the progression patterns using serial longitudinal tau PET data.

Results

We compiled an initial sample of 1,667 individuals with flortaucipir PET tau images, spanning 5 separate cohorts. A total of 1,143 individuals were identified as either cognitively normal (CN) ($n=707$) or showing biomarker evidence for A β pathology (A β +MCI, $n=223$; A β +AD dementia, $n=213$) and were used as a discovery sample for subsequent analysis. Demographic information and cross-cohort comparisons are shown in Supplementary Table 1.

Spatiotemporal subtypes of AD. We applied the SuStaIn algorithm (Extended Data Fig. 1a) to the 1,143 flortaucipir PET images to extract distinct spatiotemporal trajectories of tau spreading. As expected, many individuals ($n=700$; 61%) did not demonstrate any abnormal tau PET signal and were therefore automatically assigned to a tau⁻ group (S0) (Supplementary Note 1). Using cross-validation, we determined a four subtype solution to best represent the remaining data ($n=443$; Methods and Extended Data Fig. 1c-f). The four subtype model was applied to probabilistically assign individuals to 1 of 30 progressive stages along 1 of the 4 subtype trajectories (Fig. 1).

The distribution of clinical diagnoses across stages and subtypes can be found in Extended Data Fig. 2f,g,i. A total of 145 (32.7%) individuals exhibited a limbic-predominant phenotype with a Braak-like spatial progression across SuStaIn stages [S1: limbic]. An additional 79 individuals (17.8%) expressed a parietal-dominant and MTL-sparing phenotype, where early precuneus binding accumulated across the temporoparietal and frontal cortex but with relative sparing of the MTL [S2: MTL-sparing]. The third subtype consisted of 135 (30.5%) individuals with a predominant posterior occipitotemporal phenotype involving early occipital lobe binding and gradual anterior progression across SuStaIn stage [S3: posterior]. The remaining 84 (19.0%) individuals showed an asymmetric temporoparietal phenotype with distinct left-sided lateralization,

which was characterized by early left-temporal tau eventually spreading to the parietal and frontal cortex across disease stage [S4: lateral temporal]. The differences highlight inconsistencies between tau PET binding and pathological sequencing of specific brain regions found in previous studies, such as the hippocampus, lingual gyrus and insula^{10,11,27}, which exhibited different binding patterns across subtypes (Extended Data Fig. 3).

Stability of AD subtypes. While variation in subtype proportion was observed (and expected) across cohorts, all subtypes were represented across all cohorts (Extended Data Fig. 4). Most individuals fell neatly into the stereotypical progression of each subtype (Fig. 1b), allowing a clean stepwise progression across tau abnormality events to be observed across each subtype population (Extended Data Fig. 5). However, 12% of individuals did not fall cleanly into any subtype due to having either too little or too much pathology, both of which are uninformative for subtype (Fig. 1b and Extended Data Fig. 2d,h). In general, early-stage and individuals who were CN were assigned to subtypes with less confidence, although median subtype probability neared 100% by SuStaIn stage 7 (Extended Data Fig. 2e) and by MCI clinical stage (Extended Data Fig. 2h). This provides evidence that the earliest phases of each subtype may overlap or that they are difficult to distinguish above measurement error. We further confirmed that the subtypes produced by SuStaIn were not driven by, or specific to, arbitrary user inputs relating to the anchoring of regional pseudotimes (Methods and Extended Data Fig. 6).

We next assessed whether the same subtypes could be derived within a separate replication sample of 469 individuals scanned with the RO948 tau PET tracer. The replication cohort, BioFINDER 2 (ref. ²⁸), is described in Supplementary Table 1. SuStaIn was run separately on these individuals, constraining the analysis to produce four subtypes. Three of the four replication subtypes greatly resembled those derived in the discovery sample (Fig. 2). The only exception involved the S4: lateral temporal subtype, which had a similar overall tau PET pattern but involved right-sided rather than left-sided lateralization. Further analysis determined that this related to the smaller sample size rather than the differing radio-tracer and further suggested that the S4: lateral temporal subtype had a consistent overall pattern but a high propensity for marked lateralization (Supplementary Note 2 and Extended Data Fig. 7).

Subtypes characterized by distinct clinical profiles. Next, we compared demographic, cognitive and genetic (that is, APOE4 status) variables between the subtypes and the tau⁻ S0 group (Table 1). Individuals across all four subtypes expressed worse Mini-Mental State Examination (MMSE) and worse memory scores compared to S0 individuals. In addition, all subtypes except S1 (limbic) had worse global cognitive composite scores; individuals across all subtypes except S2 (MTL-sparing) were more likely to be APOE4 carriers and all subtypes except S4 (lateral temporal) were more likely to be female compared to S0 individuals. Compared to tau⁻ individuals in S0, S1 and S3 were older, S2 exhibited poorer executive function, S2 and S3 exhibited poorer visuospatial function and S4 had worse language scores.

Compared to other subtypes (that is, other tau⁺ individuals), individuals within the S1 (limbic) subtype were more likely to be APOE4 carriers, had less overall tau with a more right-sided pattern and had better overall cognition but worse memory relative to their overall cognition. S2 (MTL-sparing) individuals were younger, less likely to carry an APOE4 allele, had more overall tau burden, had a more right-sided tau pattern and had worse relative executive function compared to the other subtypes. S4 (lateral temporal) individuals had more overall tau with a more left-lateralized pattern. These individuals also tended to have worse overall cognition but had better relative memory and worse relative language scores

- ▲ 그림 A. 베타 일립로이드가 축적된 정상인과 좌측 베타 일립로이드가 축적되어 있는 정상인의 기능 동작화의 비교 예시. 베타 일립로이드가 축적된 사람은 일정 끝판 소프트(precunes, 후원색)의 기능적 동작화가 저하된다.
- ▲ 그림 B. 베타 일립로이드가 축적된 정상인에서 베타 일립로이드 단백질이 축적됨에 따라 기능적 동기는 쇠기 암입증, 복수 대상(anterior cingulate)부위의 기능적 동작화가 저하(파란색)된다. 반대로 기능적 이상을 보여지면서 축적된 대상의 기능적 동작화가 증강된다.

<https://www.doctorsnews.co.kr/news/articleView.html?idxno=120005>

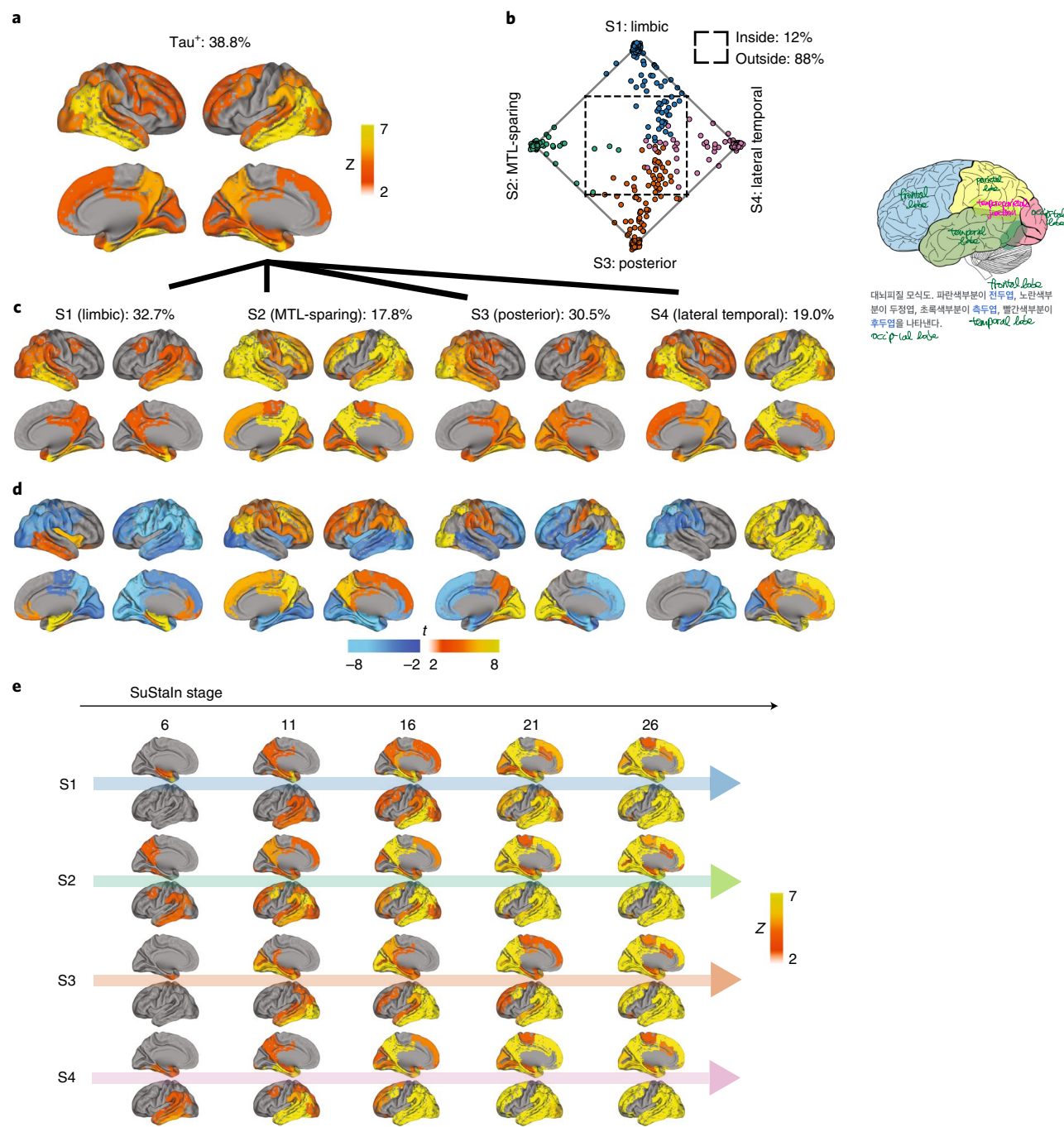


Fig. 1 | Spatiotemporal subtypes of tau progression. **a**, Tau PET pattern of tau⁺ (subtyped) individuals. **b**, Quaternary plot showing the probability each individual is classified as each subtype. The dots are labeled by final subtype classification: S1 (blue); S2 (green); S3 (orange); or S4 (pink). The inset box shows individuals who had a probability <0.5 to be classified as any of the 4 subtypes (that is, showing poor fit). **c**, Average tau PET pattern for each subtype. The color bar is the same as in **a**. **d**, Regions showing significant difference between one subtype and all other subtypes using OLS linear models adjusting for SuStAln stage, after FDR correction. **e**, Progression of each subtype through the SuStAln stages. Each image is a mean of individuals classified at the listed stage and up to four stages lower. Only the left hemisphere is shown.

compared to other subtypes. Finally, individuals with the S3 (posterior) subtype did not exhibit any significant cognitive, demographic or *APOE4* differences compared to the other subtypes. These relationships (after adjustment for demographics, diagnosis, cohort and SuStaIn stage) are described in Table 1 and visualized in Extended Data Fig. 8.

Each individual was assigned a stage along their respective subtype trajectory. As expected, increasing SuStaIn stage was associated with worse global cognition as measured with the MMSE ($r=0.54$, $P<0.0001$; Fig. 3a). This relationship was consistent across all

subtypes (S1: $r = -0.51$, S2: $r = -0.53$, S3: $r = -0.64$, S4: $r = -0.40$, all $P < 0.001$). A strong negative relationship between SuStaIn stage and age was also observed, such that individuals at the later SuStaIn stages tended to be younger ($r = -0.59$, $P < 0.0001$). This relationship was again consistent across all subtypes, although less prominent for S1 (S1: $r = -0.20$, S2: $r = -0.68$, S3: $r = -0.64$, S4: $r = -0.73$, all $P < 0.05$; Fig. 3b). This inverse relationship was also present among individuals both 65 and younger ($n = 100$, $r = -0.43$, $P < 0.0001$) and individuals older than 65 ($n = 342$, $r = -0.28$, $P < 0.0001$), suggesting the effect is not driven purely by early-onset cases. Lateralization

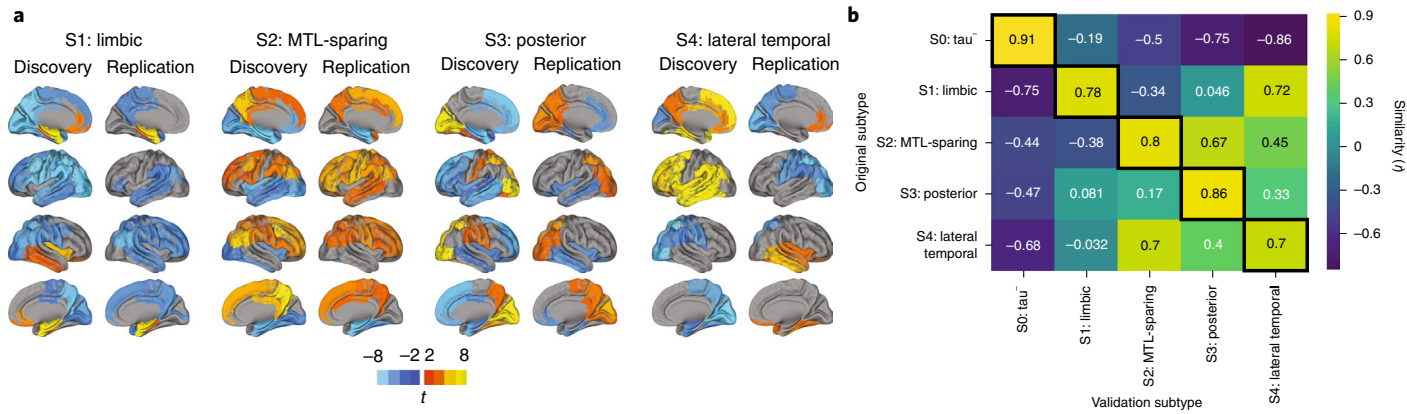


Fig. 2 | Subtype stability: AD spatiotemporal subtypes were replicated in another cohort using a different PET tracer. **a**, For both discovery and replication cohorts, the maps show regions significantly different between one subtype and all others (excluding S0) within the cohort (after FDR correction). Similar spatial patterns were observed except for a right rather than left-sided pattern in S4. **b**, Confusion matrix comparing subtypes identified in the discovery sample (y axis) and subtypes identified separately in the replication sample (x axis). Values represent spatial correlation between average regional tau-PET SUVR for each subtype. Values along the diagonal indicate similarity between the same subtype across both cohorts.

Table 1 | Comparison of means of different variables between subtypes in the discovery sample after correction for age (except in the case of age), sex (except in the case of sex), education (except in the case of education), cohort, clinical diagnosis (that is, CN, MCI, AD) and SuStAIIn stage (except comparisons with S0). Standard deviations are given in parentheses where relevant. All P values were corrected for multiple comparisons

	S0: No tau (s.d.)	S1: limbic (s.d.)	S2: MTL-sparing (s.d.)	S3: posterior (s.d.)	S4: L temporal (s.d.)
n	687	137	73	131	80
Age (years)	71.52 (8.1)	75.28 (7.7) ^a	71.34 (8.3) ^b	75.06 (7.3) ^a	73.41 (6.9)
Proportion female	0.49	0.70 ^a	0.60 ^c	0.64 ^a	0.56
Education (years)	15.17 (2.9)	14.42 (3.9)	14.29 (4.0)	14.6 (3.0)	14.82 (2.9)
Proportion APOE4 carrier	0.26	0.75 ^{a,b}	0.47 ^b	0.63 ^a	0.59 ^a
Cortical tau SUVR	1.04 (0.1)	1.41 (0.1) ^{a,b}	1.44 (0.1) ^a	1.44 (0.1) ^a	1.47 (0.1) ^{a,b}
Laterality	0.0 (0.2)	-0.28 (1.3) ^{a,b} R	-0.13 (1.6) ^{b,c} R	0.04 (1.5)	1.95 (1.2) ^{a,b} L
MMSE	28.9 (1.5)	24.33 (3.0) ^a	24.32 (4.2) ^a	24.19 (3.0) ^a	23.33 (5.0) ^a
Global cognition	0.36 (0.5)	-0.03 (0.8) ^b	-0.29 (0.8) ^a	-0.23 (0.8) ^a	-0.39 (0.9) ^{a,d}
Absolute memory	0.48 (0.7)	-0.62 (0.7) ^{a,d}	-0.36 (0.7) ^a	-0.55 (0.7) ^a	-0.3 (0.8) ^{a,d}
Absolute language	0.22 (0.7)	-0.11 (0.8)	0.01 (0.9)	-0.18 (0.8)	-0.64 (1.1) ^{a,b}
Absolute executive	0.19 (0.6)	0.02 (0.9)	-0.33 (0.9) ^a	0.03 (0.8)	-0.17 (1.0) ^c
Absolute visuospatial	0.19 (0.6)	0.08 (1.0)	-0.25 (1.2) ^a	-0.23 (1.2) ^a	-0.09 (1.0)
Relative memory	0.26 (0.8)	-0.61 (1.0) ^{a,b}	-0.14 (1.0)	-0.37 (1.0) ^a	-0.06 (1.1) ^b
Relative language	-0.02 (0.8)	0.05 (1.0)	0.31 (1.2) ^a	0.06 (1.0)	-0.51 (1.3) ^{a,b}
Relative executive	-0.14 (0.8)	0.25 (1.0) ^c	-0.22 (1.0) ^{b,c}	0.38 (1.1) ^a	0.22 (1.2)
Relative visuospatial	-0.1 (0.7)	0.31 (1.1) ^c	0.03 (1.3)	0.0 (1.3)	0.27 (1.3)

^aAdjusted $P < 0.05$ (versus S0). ^bAdjusted $P < 0.05$ (versus all other subtypes, not including S0). ^cAdjusted $P < 0.1$ (versus S0) ^dAdjusted $P < 0.1$ (versus all other subtypes, not including S0). L, significant left-sided laterality in this subtype compared to other subtypes; R, significant right-sided laterality in this subtype compared to others.

also increased with increasing SuStAIIn stage (Extended Data Fig. 9). However, despite trends in lateralization at higher SuStAIIn stages, many individuals were observed with a ‘reversed’ lateralization compared to the group average tau lateralization patterns for their subtype (Extended Data Fig. 9), suggesting lateralization to be at least partially orthogonal with subtype.

Cognitive prognosis of AD subtypes. Longitudinal MMSE data were available for a subset of 735 individuals (mean follow-up = 1.74 years from PET scan, s.d. = 0.64). Individuals with the S3 (posterior) subtype had significantly slower decline compared to all other

subtypes independently (S1: $t = 2.03$, $P = 0.043$; S2: $t = 2.88$, $P = 0.004$; S4: $t = 4.83$, $P < 0.0001$), as well as in a one-versus-all analysis ($t = 3.64$, $P = 0.0003$; Fig. 3c). This finding persisted across different clinical diagnoses (Fig. 3d and Supplementary Table 2) and was confirmed through a meta-analysis across the 5 cohorts, which also showed a significantly slower decline for the S3 (posterior) group ($t = 1.67$, $P = 0.047$; Fig. 3e). Individuals with the S4 (lateral temporal) subtype additionally showed steeper cognitive decline compared to S1 (limbic) subtype individuals ($t = 3.40$, $P = 0.0008$), and generally showed faster decline compared to other subtypes in a one-versus-all analysis ($t = -4.49$, $P < 0.0001$) and across clinical

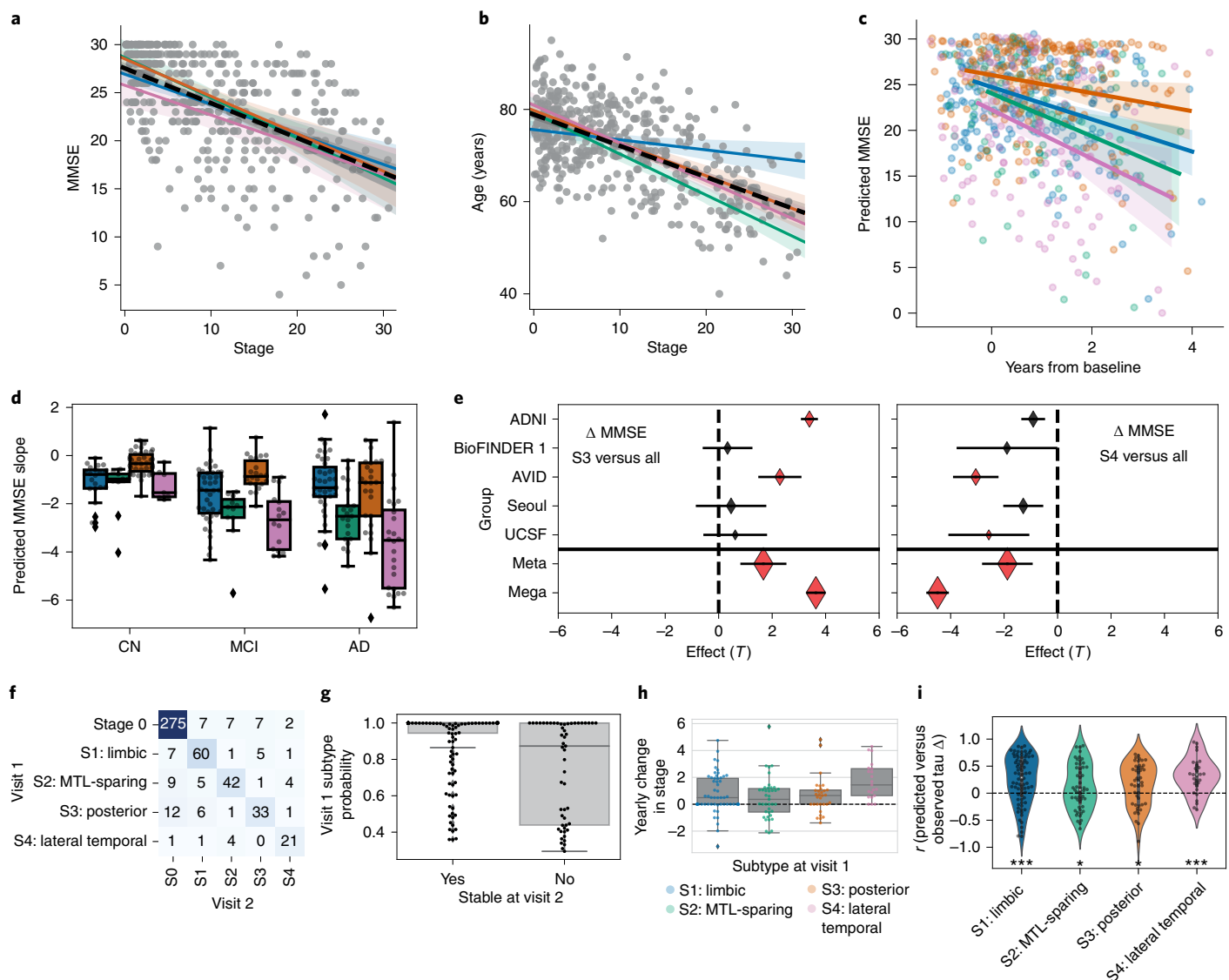


Fig. 3 | Progression of AD subtypes. **a,b**, Increasing SuStaIn stage was associated with worse cognition (**a**) and lower age (**b**) across all subtypes. **c**, Rate of longitudinal decline in MMSE for each subtype. The x axis was jittered for visualization purposes only. The y axis shows the MMSE across all observations as predicted by linear mixed models adjusted for covariates. **d**, Box plots showing the distribution of predicted MMSE slopes for each subtype, stratified by clinical diagnosis (statistics are shown in Supplementary Table 2). **e**, Cross-cohort meta-analysis for the effects of S4: lateral temporal declining faster (left) and S3: posterior declining slower (right) than other subtypes, respectively. The diamonds represent the effect sizes, while diamond size reflects relative sample size. The red diamonds indicate significant effects. Error bars, s.e.m. **f**, Confusion matrix showing longitudinal stability of subtypes. Each row shows the number of patients from a given subtype at visit 1 who were classified as each subtype at visit 2. The diagonal represents the number of patients who were classified as the same subtype at visit 1 and visit 2. **g**, Individuals with a higher probability of being classified into their subtype at baseline were more likely to show a stable subtype over time (two-sided $t(156,53) = 5.26, P = 3.6 \times 10^{-7}$). **h**, Annual change in SuStaIn stage for each subtype in individuals with stable subtypes over time (statistics are shown in Supplementary Note 3). **i**, SuStaIn was used to predict longitudinal change in regional tau accumulation. Each dot represents a patient, and the y axis represents the spatial correlation between the true and predicted regional tau change. Average predictions were significantly greater than chance based on a two-sided, one-sample t -test against 0 (S1: $t(78) = 5.00, P = 3.5 \times 10^{-6}$; S2: $t(52) = 2.16, P = 0.035$; S3: $t(45) = 3.05, P = 0.0039$; S4: $t(29) = 4.93, P = 3.1 \times 10^{-5}$). * $P_{\text{unc}} < 0.05$, ** $P_{\text{unc}} < 0.001$. **a-c**, The error bars represent the 95% confidence interval of the model fit across 1,000 bootstrap samples. For the box plots in **d,g-i**, the center line is the median, the box represents the inner quartiles, the whiskers represent the extent of data distribution except for the outliers (signified by the asterisks).

diagnoses (Fig. 3d and Supplementary Table 2). A meta-analysis once again confirmed a significant overall effect ($t=1.88, P=0.031$; Fig. 3e).

Stability and progression of AD subtypes over time. SuStaIn uses cross-sectional data to infer longitudinal trajectories for the tau data, so evaluating how well longitudinal data fits the model is a key aspect of validation. A total of 519 individuals from the discovery

sample also had follow-up floratacipur PET scans (mean follow-up time = 1.42 years, s.d. = 0.58). Overall, 88.5% of individuals exhibited the same subtype at both baseline and follow-up or progressed from S0 into a subtype (Fig. 3f). Stability when excluding individuals classified as S0 at baseline (tau⁺ stability) and follow-up was 83.9%. Stable individuals were classified with a higher degree of confidence at baseline compared to individuals whose subtype changed at follow-up (stable mean = 0.91, s.d. = 0.17; change

mean = 0.74, s.d. = 0.27; $t = 5.26$, $P < 0.0001$; Fig. 3g). Supplementary Table 3 shows longitudinal tau⁺ stability (that is, excluding S0) when excluding individuals using various subtype probability thresholds.

We next examined how SuStaIn stage changed over time for each subtype. Across the whole sample, we observed significant yearly increase in SuStaIn stage (mean Δ/year = 0.8, $t(148) = 6.54$, $P < 0.0001$) (Fig. 3h and Supplementary Table 4); a significant difference in mean annual rate of SuStaIn stage change was seen across subtypes (Supplementary Note 3). The annual SuStaIn stage increased faster in S4 (lateral temporal) compared to S2 (MTL-sparing) and S3 (posterior) subtypes (Fig. 3h and Supplementary Note 3). Younger age ($r = -0.22$, $P = 0.006$) but not higher baseline SuStaIn stage ($r = 0.12$, $P = 0.15$) was associated with faster annual change in stage. As a final validation, we used SuStaIn to forecast the longitudinal rate of regional tau PET change at the individual level. On average, predictions were significantly better than chance for all subtypes (S1 (limbic): $t(78) = 5.00$, $P < 0.0001$; S2 (MTL-sparing): $t(52) = 2.16$, $P = 0.035$; S3 (posterior): $t(45) = 3.05$, $P = 0.0039$; S4 (lateral temporal): $t(29) = 4.93$, $P < 0.0001$; Fig. 3i).

Subtype patterns resemble distinct corticolimbic networks. Based on our previous work²⁹, we used network diffusion models to examine the possibility that the observed subtype-specific tau spreading patterns may be driven by spread through distinct networks. We found that an entorhinal cortex epicenter was optimal for the S1 (limbic) subtype tau pattern and strongly replicated the pattern of tau spreading ($r^2 = 0.70$) but did not reproduce other subtype patterns nearly as well (S2: $r^2 = 0.04$; S3: $r^2 = 0.41$; S4: $r^2 = 0.37$). Models using different epicenters substantially improved the fit for these other subtypes (Fig. 4a,b,e): best-fitting models used the middle temporal gyrus ($r^2 = 0.27$) for S2 (MTL-sparing), the fusiform gyrus ($r^2 = 0.59$) for S3 (posterior) and the inferior temporal gyrus ($r^2 = 0.50$) for S4 (L Temporal) (Fig. 4c), suggesting a possible predominance of these regions in secondary tau seeding for different subtypes. Highly similar results were found using a different brain atlas and different connectivity data (Extended Data Fig. 10). We further tracked how the best-fitting epicenter changed at higher disease stages, perhaps reflecting participation of different regions as secondary seeding points with advancing disease progression (Fig. 4d). All but the S2 (MTL-sparing) subtype exhibited MTL spreading in the earlier stages, whereas the early stages of S2 involved parietal spread. Later stages involved secondary seeding in the temporal lobes and subtype-specific regions. Together, these results suggest that distinct tau patterns across different subtypes may be driven in part by vulnerability of, or selective spread through, distinct temporal lobe networks.

Discussion

For the last 30 years, the progression of tau pathology in AD has principally been described by a single model of spatiotemporal evolution^{8,9} despite frequent examples of nonconforming cases¹². We showed that the cortical cascade of tau pathology is better described by a data-driven model including multiple spatiotemporal patterns (Fig. 5). Importantly, our findings may reconcile atypical AD variants with common variations of typical AD into a single unified model of pathological progression. First, the model reaffirms the existence of observed cortical- and limbic-predominant pathological patterns as distinct subtypes of tau progression rather than phases along a continuum. In addition, the model also accounts for the most frequently occurring atypical clinical variants of AD, PCA and logopenic PPA as the extremes of regularly occurring posterior and lateral temporal AD subtypes. Together, our data align with a recent model¹⁴ to suggest variation in the pathological expression of AD along two orthogonal axes, subtype and severity, the latter of which is strongly and inversely correlated with age (Fig. 5). Given that no dominant pattern emerged, our data suggest the existence of

multiple common AD subtypes, challenging the notion that there is such a pathological entity that can be described as 'typical' AD. Rather, the spatial pattern of tau spreading appears to vary along at least four archetypes, depending on factors such as age and genotype. Therefore, we propose that heterogeneity in AD is best represented as a quadrilateral axis (Fig. 5).

Our results are robust across datasets and radiotracers. We found individuals representing each of four subtype patterns in each of the five contributing cohorts and reproduced a very similar set of subtypes in a totally separate sample using a different radiotracer. Furthermore, most individuals were confidently assigned into one subtype pattern, which was consistent over time. The limbic subtype was the most frequent and presented with many characteristics typically associated with AD, including a greater proportion of APOE4 carriers, a strongly amnestic phenotype and medial temporal pathology with a Braak-like progression of tau spread. However, this subtype represented only a third of all tau⁺ cases in our dataset (although the earliest stages of three of the four subtypes featured prominent MTL binding; Fig. 4d). Instead, our data suggest that, at an older age at onset or earlier disease stages, subtypes may present with subtle differences that may be difficult to detect in the clinic, while at a younger age at onset or later disease stages, the more aggressive phenotype can amplify the distinct subtype expressions. The existence of these phenotypes, if further validated, may necessitate a reform in pathological tau staging, where key regions are surveyed to increase sensitivity to detect subtype-specific patterns.

Many pioneering studies have noted variation in AD pathology. For example, limbic-predominant and MTL-sparing phenotypes are contrasted against 'typical' phenotypes that express tau pathology in both the MTL and neocortex^{12,13}. In contrast to this notion, we found that a subtype of individuals expressing both cortical and MTL tau exhibited a more aggressive phenotype with marked lateralization, the latter being a feature that has not been well characterized in histopathological studies of AD, which typically assess only one hemisphere. In addition, our model allows the concurrence of MTL and cortical pathology at later stages of several distinct progressions, perhaps suggesting that solely contrasting cortical and MTL tau (for example, see refs. ^{21,22}) may not be sufficient to describe AD heterogeneity. Indeed, while some spatial convergence could be observed in our AD subtypes, particularly at the early or late stages, subtle regional variation consistently distinguished individuals of one subtype from another.

We reproduce previous reports describing a strong negative correlation between age and tau progression^{30–34}, as well as previous reports that a younger age at onset of AD is associated with a more rapid progression of tau pathology^{35,36}. Interestingly, in our study, this phenomenon was observable across all subtypes (Fig. 3b). Previous work has noted that early-onset AD is more likely to present with an atypical (that is, nonamnestic) phenotype³⁷. This may be a specific characteristic of early-onset AD. However, ours and other studies^{26,38,39} suggest that posterior or left-lateralized temporal binding is not uncommon across the age spectrum, although our data suggest that the phenotype is more pronounced at the earlier ages. Therefore, atypical variants of AD may represent an accelerated and intensified manifestation of common AD subtypes, although this will require further validation.

Our findings complement other supervised and unsupervised AD subtyping studies from the imaging and pathology literature^{12–14,21,22,26,38}, although our analysis also produced some new findings that are worthy of further investigation. Despite the extreme of the posterior subtype being represented by PCA, an aggressive disease variant, the posterior subtype overall demonstrated slower cognitive decline compared to all other subtypes. These individuals exhibited considerable tau pathology in posterior (including occipital) brain regions but also relatively less MTL and frontal binding. However, these findings are in agreement with the pathology

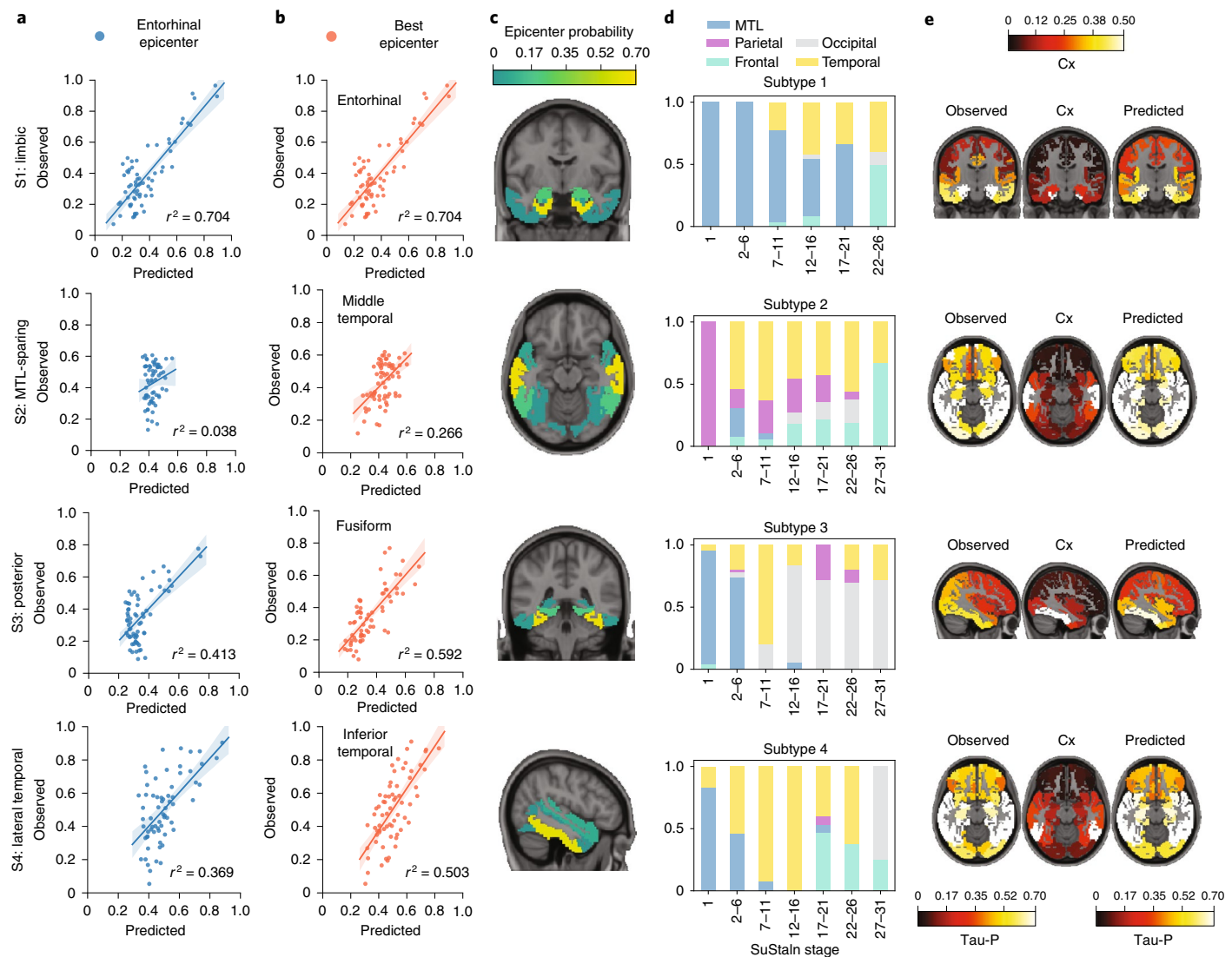


Fig. 4 | Application of epidemic spreading model to determine subtype-specific corticolimbic circuit vulnerability. **a,b**, An epidemic spreading model was fitted separately for each subtype; once using an entorhinal cortex epicenter (**a**, blue) and once with a subtype-specific best-fitting epicenter (**b**, red). For each plot, each dot represents a region. The x axis represents the mean simulated tau⁺ probabilities across the population, while the y axis represents the mean observed tau⁺ probability. Each row represents a subtype. **a-c**, The error bars represent the 95% CI of model fitting across 1,000 bootstrap samples. **c**, For each subtype, the probability that each region was the best-fitting epicenter for that subtype is shown, which was based on bootstrap resampling. **d**, For each subtype, the proportion of individuals at various stages that had best-fitting epicenters within each of five major brain divisions is shown: MTL (blue); temporal lobe (yellow); parietal lobe (purple); occipital lobe (gray); and frontal lobe (turquoise). **e**, For each subtype, spatial representation of the ESM results from **b** using the best-fitting epicenter is shown. From left to right, observed regional tau PET probabilities (tau-P), regional connectivity to best-fitting epicenter (Cx) and tau PET probabilities predicted by the ESM. These images show the degree to which constrained diffusion of signal through a connectome (predicted), starting in a given epicenter and its associated fiber network (Cx), recapitulates the tau patterns of each subtype (observed).

literature describing common variation in occipital tau pathology in both preclinical and symptomatic AD^{2,40–42}. These studies, variously surveying Brodmann areas 17, 18 and 19, found evidence for occipital lobe tau in 24–52% of sampled brains, including in individuals who were CN. Our study suggests this population variation may indeed be systematic and could be associated with a specific progression pattern. However, tau in the occipital lobe remains understudied and future studies will be necessary to validate the precise characteristics of this posterior subtype. It is still unclear if the posterior subtype is related to PCA beyond a shared predominance of posterior tau, although it may at least signify the existence of a posterior cortical network selectively vulnerable to tau pathology.

Different manifestations of AD may represent subtle variations in the spread of pathology or could signal the influence of highly

distinct processes relevant to treatment intervention. For example, a recent pathology study found increased neurofibrillary tangle pathology and neuronal loss in the cholinergic basal forebrain specifically in patients with an MTL-sparing phenotype and that earlier disease onset was associated with more neurofibrillary tangle pathology in these individuals⁴³. Furthermore, another recent study indicated that a targeted basal forebrain treatment could be most effective for patients with an MTL-sparing phenotype⁴⁴. This research may suggest a unique role of the basal forebrain in certain subtypes of AD. Meanwhile, APOE has been consistently associated with limbic manifestations of AD^{12,34}, including the present study, and APOE or hippocampus-focused therapies could prove more effective for these individuals. Together, these results point to the possibility that clinical trials may benefit from stratification or

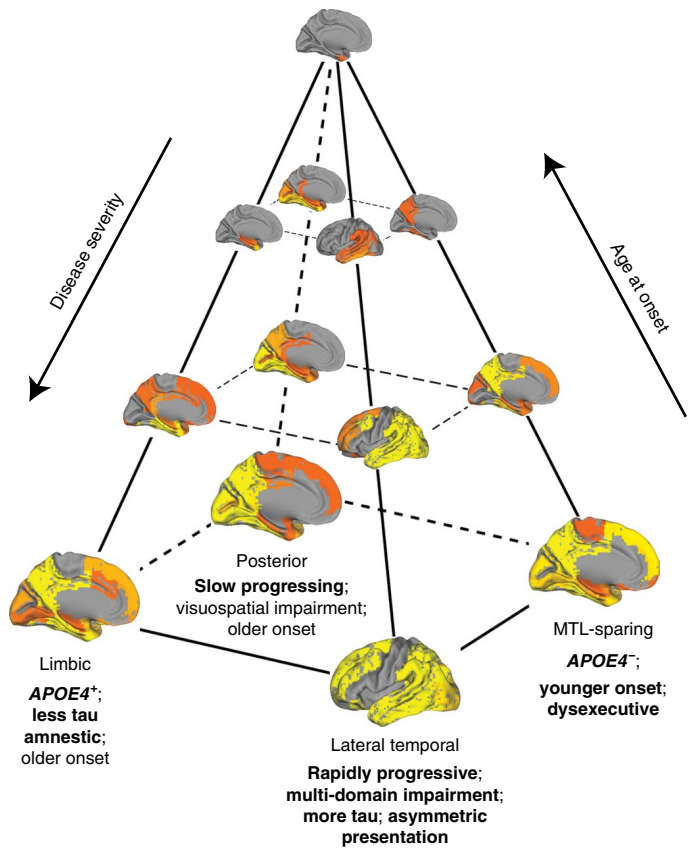


Fig. 5 | A theoretical model summarizing variation in the spread of tau pathology in AD. Tau pathology varies along an axis of severity (vertical in the diagram), which is inversely associated with age at onset. Tau varies along a spatiotemporal dimension (horizontal plane in the diagram), such that an individual can be described by their fit along one of at least four trajectories. The text indicates the clinical characteristics of each subtype. The text in bold reflects robust differences between subtypes, while normal text reflects less robust characteristics that differentiate subtypes from tau⁻ individuals.

enrichment based on AD subtype, or as a first step, post hoc identification of within-subtype effects.

There are currently very few explanations as to why subtypes of AD manifest. Fascinating work has found that PCA and logopenic PPA patients are more likely to exhibit learning disabilities in childhood^{45,46}, perhaps mediated by abnormalities during brain development⁴⁷. While logopenic PPA and PCA may represent extremes along the AD continuum (as indicated by the present results), this points to the possibility that distinct subtypes may be influenced by variation in cognitive development or other premorbid factors. Interactions between posttranslational tau modification and synaptic tau spreading are another possible explanation for subtypes. Several studies have shown that the regional pattern of pathological tau expression in mice is dependent on the conformation and injection site of tau seeds^{35,48,49}. Therefore, it is possible that subtypes of tau spread may simply be dictated by distinct tau conformations and/or systematic variation in the human connectome, perhaps at key synaptic junctures. Supporting the latter hypothesis, we found that the tau PET pattern of AD subtypes resembled macroscale neuronal networks seeded from different brain regions. These findings do not presuppose tau pathology necessarily starts in different regions but instead that different regions may play a more prominent role in tau propagation across subtypes as ‘amplifying nodes’. This could be mediated by involvement of distinct neuronal cell

subtypes⁵⁰, which may incur disrupted development due to environmental or genetic factors, leading to network abnormality during life and network vulnerability in later life.

This study has a number of limitations. The SuStaIn method fits data based on the assumption that several discrete sequences are represented within the data and uses cross-sectional information to create pseudo-longitudinal sequences. This framework is based on the same logic as most pathological staging schema (for example, Braak and Braak⁸) and hypotheses of biomarker trajectories (for example, Jack et al.⁵) but does so in an automated fashion. Therefore, it is possible that a SuStaIn subtype trajectory could be created by ‘appending’ or ‘stitching’ unrelated disease states together. However, we found that most individuals remained the same subtype at longitudinal follow-up and we could predict regional individual tau accumulation greater than by chance using just the SuStaIn model. While the use of tau PET imaging is a great improvement over using magnetic resonance imaging to measure AD pathology, there is still some discrepancy between the tau PET signal and true tau pathology⁵¹. While flortaucipir binds to paired helical filament tau, off-target binding is an issue with flortaucipir, particularly in the striatum, white matter and choroid plexus⁵². We mitigated this issue by regression of choroid plexus signal, exclusion of subcortical regions of interest (ROIs) and non-AD dementia patients and region-specific normalization against nonspecific binding, as well as replication with RO948, which exhibits less off-target binding⁵³. Similarly, recent reports questioned whether elevated flortaucipir binding is detectable before advanced stages of tau accumulation^{54–56}. However, SuStaIn modeling is based on relative regional differences in pathology and regional variation in tau PET and tau pathology are correlated^{55–57}. Still, while the unbiased spatial sampling of tau PET data across the brain aided our discovery of these subtype patterns, they must still be validated using histopathology studies. Sample size was an obvious strength of our study but it comes with the caveat of mixing data from multiple cohorts, scanners and cognitive batteries. We addressed this issue somewhat by examining subtypes in each cohort separately, replicating our results in a separate sample and adjusting for cohort in our comparisons. In addition, despite our study boasting the largest tau PET sample to date, even larger samples would be preferable to elucidate the spatiotemporal progression of each subtype in more detail. We arrived at a four subtype solution to describe our data using established statistical methodology to identify a solution the data support with confidence. However, this does not preclude the possibility that other, more subtly distinct subtypes exist (Extended Data Fig. 1f).

In conclusion, we describe four distinct but stable spatiotemporal phenotypes of tau accumulation in AD. These subtypes exhibit differing clinical profiles and longitudinal outcomes and their tau patterns resemble distinct temporal lobe networks. Our data-driven results call into question whether ‘typical AD’ is a quantifiable entity, rather suggesting that several AD subtypes exist and that their individual differences are exacerbated by more aggressive phenotypes with younger ages at onset. Future studies should seek to validate the existence and temporal evolution of these subtypes, as well as identify genetic, cellular and developmental factors that may influence their expression. This may include identifying differences in brain activity and connectivity between individuals, as well as differences in regional vulnerability. This framework may also be useful to enrich clinical trials, provide more individualized clinical care and eventually more individualized treatment.

Online content

Any methods, additional references, Nature Research reporting summaries, source data, extended data, supplementary information, acknowledgements, peer review information; details of author contributions and competing interests; and statements of

data and code availability are available at <https://doi.org/10.1038/s41591-021-01309-6>.

Received: 20 August 2020; Accepted: 4 March 2021;

Published online: 29 April 2021

References

- Hurd, M. D., Martorell, P., Delavande, A., Mullen, K. J. & Langa, K. M. Monetary costs of dementia in the United States. *N. Engl. J. Med.* **368**, 1326–1334 (2013).
- Alafuzoff, I. et al. Staging of neurofibrillary pathology in Alzheimer's disease: a study of the BrainNet Europe Consortium. *Brain Pathol.* **18**, 484–496 (2008).
- Hyman, B. T. et al. National Institute on Aging—Alzheimer's Association guidelines for the neuropathologic assessment of Alzheimer's disease. *Alzheimers Dement.* **8**, 1–13 (2012).
- Hardy, J. & Selkoe, D. J. The amyloid hypothesis of Alzheimer's disease: progress and problems on the road to therapeutics. *Science* **297**, 353–356 (2002).
- Jack, C. R. Jr et al. Tracking pathophysiological processes in Alzheimer's disease: an updated hypothetical model of dynamic biomarkers. *Lancet Neurol.* **12**, 207–216 (2013).
- La Joie, R. et al. Prospective longitudinal atrophy in Alzheimer's disease correlates with the intensity and topography of baseline tau-PET. *Sci. Transl. Med.* **12**, eaau5732 (2020).
- Bejanin, A. et al. Tau pathology and neurodegeneration contribute to cognitive impairment in Alzheimer's disease. *Brain* **140**, 3286–3300 (2017).
- Braak, H. & Braak, E. Neuropathological staging of Alzheimer-related changes. *Acta Neuropathol.* **82**, 239–259 (1991).
- Braak, H., Alafuzoff, I., Arzberger, T., Kretzschmar, H. & Del Tredici, K. Staging of Alzheimer disease-associated neurofibrillary pathology using paraffin sections and immunocytochemistry. *Acta Neuropathol.* **112**, 389–404 (2006).
- Schöll, M. et al. PET imaging of tau deposition in the aging human brain. *Neuron* **89**, 971–982 (2016).
- Schwarz, A. Regional profiles of the candidate tau PET ligand ¹⁸F-AV-1451 recapitulate key features of Braak histopathological stages. *Brain* **139**, 1539–1550 (2016).
- Murray, M. E. et al. Neuropathologically defined subtypes of Alzheimer's disease with distinct clinical characteristics: a retrospective study. *Lancet Neurol.* **10**, 785–796 (2011).
- Whitwell, J. L. et al. Neuroimaging correlates of pathologically defined subtypes of Alzheimer's disease: a case-control study. *Lancet Neurol.* **11**, 868–877 (2012).
- Ferreira, D., Nordberg, A. & Westman, E. Biological subtypes of Alzheimer's disease: a systematic review and meta-analysis. *Neurology* **94**, 436–448 (2020).
- Ossenkoppelaar, R. et al. Tau PET patterns mirror clinical and neuroanatomical variability in Alzheimer's disease. *Brain* **139**, 1551–1567 (2016).
- Crutch, S. J. et al. Consensus classification of posterior cortical atrophy. *Alzheimers Dement.* **13**, 870–884 (2017).
- Gorno-Tempini, M. L. et al. Classification of primary progressive aphasia and its variants. *Neurology* **76**, 1006–1014 (2011).
- Ossenkoppelaar, R. et al. The behavioural/dysexecutive variant of Alzheimer's disease: clinical, neuroimaging and pathological features. *Brain* **138**, 2732–2749 (2015).
- Drummond, E. et al. Proteomic differences in amyloid plaques in rapidly progressive and sporadic Alzheimer's disease. *Acta Neuropathol.* **133**, 933–954 (2017).
- Crist, A. M. et al. Leveraging selective hippocampal vulnerability among Alzheimer's disease subtypes reveals a novel tau binding partner SERPINA5. Preprint at *bioRxiv* <https://doi.org/10.1101/2020.12.18.423469> (2020).
- Risacher, S. L. et al. Alzheimer disease brain atrophy subtypes are associated with cognition and rate of decline. *Neurology* **89**, 2176–2186 (2017).
- Ossenkoppelaar, R. et al. Distinct tau PET patterns in atrophy-defined subtypes of Alzheimer's disease. *Alzheimers Dement.* **16**, 335–344 (2020).
- Young, A. L. et al. Uncovering the heterogeneity and temporal complexity of neurodegenerative diseases with Subtype and Stage Inference. *Nat. Commun.* **9**, 4273 (2018).
- Dong, A. et al. Heterogeneity of neuroanatomical patterns in prodromal Alzheimer's disease: links to cognition, progression and biomarkers. *Brain* **140**, 735–747 (2017).
- Noh, Y. et al. Anatomical heterogeneity of Alzheimer disease: based on cortical thickness on MRIs. *Neurology* **83**, 1936–1944 (2014).
- Tam, A. et al. A highly predictive signature of cognition and brain atrophy for progression to Alzheimer's dementia. *Gigascience* **8**, giz055 (2019).
- Vogel, J. W. et al. Data-driven approaches for tau-PET imaging biomarkers in Alzheimer's disease. *Hum. Brain Mapp.* **40**, 638–651 (2019).
- Leuzy, A. et al. Diagnostic performance of RO948 F 18 tau positron emission tomography in the differentiation of Alzheimer disease from other neurodegenerative disorders. *JAMA Neurol.* **77**, 955–965 (2020).
- Vogel, J. W. et al. Spread of pathological tau proteins through communicating neurons in human Alzheimer's disease. *Nat. Commun.* **11**, 2612 (2020).
- Marshall, G. A., Fairbanks, L. A., Tekin, S., Vinters, H. V. & Cummings, J. L. Early-onset Alzheimer's disease is associated with greater pathologic burden. *J. Geriatr. Psychiatry Neurol.* **20**, 29–33 (2007).
- Whitwell, J. L. et al. The role of age on tau PET uptake and gray matter atrophy in atypical Alzheimer's disease. *Alzheimers Dement.* **15**, 675–685 (2019).
- Pontecorvo, M. J. et al. A multicentre longitudinal study of flortaucipir (¹⁸F) in normal ageing, mild cognitive impairment and Alzheimer's disease dementia. *Brain* **142**, 1723–1735 (2019).
- Jack, C. R. et al. Predicting future rates of tau accumulation on PET. *Brain* **143**, 3136–3150 (2020).
- La Joie, R. et al. Association of APOE4 and clinical variability in Alzheimer disease with the pattern of tau- and amyloid-PET. *Neurology* **96**, e650–e661 (2021).
- Dujardin, S. et al. Tau molecular diversity contributes to clinical heterogeneity in Alzheimer's disease. *Nat. Med.* **26**, 1256–1263 (2020).
- Aoyagi, A. et al. Aβ and tau prion-like activities decline with longevity in the Alzheimer's disease human brain. *Sci. Transl. Med.* **11**, eaat8462 (2019).
- Koedam, E. L. G. E. et al. Early-versus late-onset Alzheimer's disease: more than age alone. *J. Alzheimers Dis.* **19**, 1401–1408 (2010).
- Sun, N., Mormino, E. C., Chen, J., Sabuncu, M. R. & Yeo, B. T. T. Multi-modal latent factor exploration of atrophy, cognitive and tau heterogeneity in Alzheimer's disease. *NeuroImage* **201**, 116043 (2019).
- Franzmeier, N. et al. Patient-centered connectivity-based prediction of tau pathology spread in Alzheimer's disease. *Sci. Adv.* **6**, eabd1327 (2020).
- Mukaetova-Ladinska, E. B. et al. Regional distribution of paired helical filaments and normal tau proteins in aging and in Alzheimer's disease with and without occipital lobe involvement. *Dement. Geriatr. Cogn. Disord.* **3**, 61–69 (1992).
- McKee, A. C. et al. Visual association pathology in preclinical Alzheimer disease. *J. Neuropathol. Exp. Neurol.* **65**, 621–630 (2006).
- Pikkarainen, M., Kauppinen, T. & Alafuzoff, I. Hyperphosphorylated tau in the occipital cortex in aged nondemented subjects. *J. Neuropathol. Exp. Neurol.* **68**, 653–660 (2009).
- Hanna-Al-Shaikh, F. S. et al. Selective vulnerability of the nucleus basalis of Meynert among neuropathologic subtypes of Alzheimer disease. *JAMA Neurol.* **77**, 225–233 (2019).
- Machado, A. et al. The cholinergic system in subtypes of Alzheimer's disease: an in vivo longitudinal MRI study. *Alzheimers Res. Ther.* **12**, 51 (2020).
- Rogalski, E., Johnson, N., Weintraub, S. & Mesulam, M. Increased frequency of learning disability in patients with primary progressive aphasia and their first-degree relatives. *Arch. Neurol.* **65**, 244–248 (2008).
- Ossenkoppelaar, R. et al. Discriminative accuracy of [¹⁸F]flortaucipir positron emission tomography for Alzheimer disease vs other neurodegenerative disorders. *JAMA* **320**, 1151–1162 (2018).
- Miller, Z. A. Cortical developmental abnormalities in logopenic variant primary progressive aphasia with dyslexia. *Brain Commun.* **1**, fc027 (2019).
- Hyman, B. T. Tau propagation, different tau phenotypes, and prion-like properties of tau. *Neuron* **82**, 1189–1190 (2014).
- He, Z. et al. Transmission of tauopathy strains is independent of their isoform composition. *Nat. Commun.* **11**, 7 (2020).
- Leng, K. et al. Molecular characterization of selectively vulnerable neurons in Alzheimer's disease. *Nat. Neurosci.* **24**, 276–287 (2021).
- Lemoine, L., Leuzy, A., Chiotis, K., Rodriguez-Vieitez, E. & Nordberg, A. Tau positron emission tomography imaging in tauopathies: the added hurdle of off-target binding. *Alzheimers Dement. (Amst.)* **10**, 232–236 (2018).
- Baker, S. L., Harrison, T. M., Maaf, A., La Joie, R. & Jagust, W. Effect of off-target binding on ¹⁸F-flortaucipir variability in healthy controls across the lifespan. *J. Nucl. Med.* <https://doi.org/10.2967/jnumed.118.224113> (2019).
- Smith, R. et al. Head-to-head comparison of tau positron emission tomography tracers [¹⁸F]flortaucipir and [¹⁸F]RO948. *Eur. J. Nucl. Med. Mol. Imaging* **47**, 342–354 (2020).
- Fleisher, A. S. et al. Positron emission tomography imaging with [¹⁸F]flortaucipir and postmortem assessment of Alzheimer disease neuropathologic changes. *JAMA Neurol.* **77**, 829–839 (2020).
- Lowe, V. J. et al. Tau-positron emission tomography correlates with neuropathology findings. *Alzheimers Dement.* **16**, 561–571 (2020).
- Soleimani-Meigooni, D. N. et al. ¹⁸F-flortaucipir PET to autopsy comparisons in Alzheimer's disease and other neurodegenerative diseases. *Brain* **143**, 3477–3494 (2020).
- Smith, R., Wibom, M., Pawlik, D., Englund, E. & Hansson, O. Correlation of in vivo [¹⁸F]flortaucipir with postmortem Alzheimer disease Tau pathology. *JAMA Neurol.* **76**, 310–317 (2019).

Publisher's note Springer Nature remains neutral with regard to jurisdictional claims in published maps and institutional affiliations.

© The Author(s), under exclusive licence to Springer Nature America, Inc. 2021

the Alzheimer's Disease Neuroimaging Initiative

Michael Weiner¹⁶, Paul Aisen¹⁷, Ronald Petersen¹⁸, Clifford R. Jack Jr.¹⁸, William Jagust¹⁹, John Q. Trojanowski²⁰, Arthur W. Toga²¹, Laurel Beckett²², Robert C. Green²³, Andrew J. Saykin²⁴, John Morris²⁵, Leslie M. Shaw²⁰, Enchi Liu²⁶, Tom Montine²⁷, Ronald G. Thomas¹⁷, Michael Donohue¹⁷, Sarah Walter¹⁷, Devon Gessert¹⁷, Tamie Sather¹⁷, Gus Jiminez¹⁷, Danielle Harvey²², Matthew Bernstein¹⁸, Nick Fox²⁸, Paul Thompson²⁹, Norbert Schuff³⁰, Charles DeCarli²², Bret Borowski¹⁸, Jeff Gunter¹⁸, Matt Senjem¹⁸, Prashanthi Vemuri¹⁸, David Jones¹⁸, Kejal Kantarci¹⁸, Chad Ward¹⁸, Robert A. Koepp³¹, Norm Foster³², Eric M. Reiman³³, Kewei Chen³³, Chet Mathis³⁴, Susan Landau¹⁹, Nigel J. Cairns²⁵, Erin Householder²⁵, Lisa Taylor Reinwald²⁵, Virginia Lee³⁵, Magdalena Korecka³⁵, Michal Figurski³⁵, Karen Crawford²¹, Scott Neu²¹, Tatiana M. Foroud²⁴, Steven Potkin³⁶, Li Shen²⁴, Faber Kelley²⁴, Sungeun Kim²⁴, Kwangsik Nho²⁴, Zaven Kachaturian³⁷, Richard Frank³⁸, Peter J. Snyder³⁹, Susan Molchan⁴⁰, Jeffrey Kaye⁴¹, Joseph Quinn⁴¹, Joseph Quinn⁴¹, Betty Lind⁴¹, Raina Carter⁴¹, Sara Dolen⁴¹, Lon S. Schneider²¹, Sonia Pawluczyk²¹, Mauricio Beccera²¹, Liberty Teodoro²¹, Bryan M. Spann²¹, James Brewer¹⁷, Helen Vanderswag¹⁷, Adam Fleisher³³, Judith L. Heidebrink³¹, Joanne L. Lord³¹, Sara S. Mason¹⁸, Colleen S. Albers¹⁸, David Knopman¹⁸, Kris Johnson¹⁸, Rachelle S. Doody⁴², Javier Villanueva Meyer⁴², Munir Chowdhury⁴², Susan Rountree⁴², Mimi Dang⁴², Yaakov Stern⁴³, Lawrence S. Honig⁴³, Karen L. Bell⁴³, Beau Ances⁴⁴, John C. Morris⁴⁴, Maria Carroll⁴⁴, Sue Leon⁴⁴, Mark A. Mintun⁴⁴, Stacy Schneider⁴⁴, Angela Oliver⁴⁵, Randall Griffith⁴⁵, David Clark⁴⁵, David Geldmacher⁴⁵, John Brockington⁴⁵, Erik Roberson⁴⁵, Hillel Grossman⁴⁶, Effie Mitsis⁴⁶, Leyla de Toledo-Morrell⁴⁷, Raj C. Shah⁴⁷, Ranjan Duara⁴⁸, Daniel Varon⁴⁸, Maria T. Greig⁴⁸, Peggy Roberts⁴⁸, Marilyn Albert⁴⁹, Chiadi Onyike⁴⁹, Daniel D'Agostino II⁴⁹, Stephanie Kielb⁴⁹, James E. Galvin⁵⁰, Dana M. Pogorelec⁵⁰, Brittany Cerbone⁵⁰, Christina A. Michel⁵⁰, Henry Rusinek⁵⁰, Mony J. de Leon⁵⁰, Lidia Glodzik⁵⁰, Susan De Santi⁵⁰, P. Murali Doraiswamy⁵¹, Jeffrey R. Petrella⁵¹, Terence Z. Wong⁵¹, Steven E. Arnold²⁰, Jason H. Karlawish²⁰, David Wolk²⁰, Charles D. Smith⁵², Greg Jicha⁵², Peter Hardy⁵², Partha Sinha⁵², Elizabeth Oates⁵², Gary Conrad⁵², Oscar L. Lopez³⁴, MaryAnn Oakley³⁴, Donna M. Simpson³⁴, Anton P. Porsteinsson⁵³, Bonnie S. Goldstein⁵³, Kim Martin⁵³, Kelly M. Makino⁵³, M. Saleem Ismail⁵³, Connie Brand⁵³, Ruth A. Mulnard⁵⁴, Gaby Thai⁵⁴, Catherine McAdams Ortiz⁵⁴, Kyle Womack⁵⁵, Dana Mathews⁵⁵, Mary Quiceno⁵⁵, Ramon Diaz Arrastia⁵⁵, Richard King⁵⁵, Myron Weiner⁵⁵, Kristen Martin Cook⁵⁵, Michael DeVous⁵⁵, Allan I. Levey⁵⁶, James J. Lah⁵⁶, Janet S. Cellar⁵⁶, Jeffrey M. Burns⁵⁷, Heather S. Anderson⁵⁷, Russell H. Swerdlow⁵⁷, Liana Apostolova⁵⁸, Kathleen Tingus⁵⁸, Ellen Woo⁵⁸, Daniel H. S. Silverman⁵⁸, Po H. Lu⁵⁸, George Bartzokis⁵⁸, Neill R. Graff Radford⁵⁹, Francine Parfitt⁵⁹, Tracy Kendall⁵⁹, Heather Johnson⁵⁹, Martin R. Farlow²⁴, Ann Marie Hake²⁴, Brandy R. Matthews²⁴, Scott Herring²⁴, Cynthia Hunt²⁴, Christopher H. van Dyck⁶⁰, Richard E. Carson⁶⁰, Martha G. MacAvoy⁶⁰, Howard Chertkow⁶¹, Howard Bergman⁶¹, Chris Hosein⁶¹, Sandra Black⁶², Bojana Stefanovic⁶², Curtis Caldwell⁶², Ging Yuek Robin Hsiung⁶³, Howard Feldman⁶³, Benita Mudge⁶³, Michele Assaly Past⁶³, Andrew Kertesz⁶⁴, John Rogers⁶⁴, Dick Trost⁶⁴, Charles Bernick⁶⁵, Donna Munic⁶⁵, Diana Kerwin⁶⁶, Marek Marsel Mesulam⁶⁶, Kristine Lipowski⁶⁶, Chuang Kuo Wu⁶⁶, Nancy Johnson⁶⁶, Carl Sadowsky⁶⁷, Walter Martinez⁶⁷, Teresa Villena⁶⁷, Raymond Scott Turner⁶⁸, Kathleen Johnson⁶⁸, Brigid Reynolds⁶⁸, Reisa A. Sperling²³, Keith A. Johnson²³, Gad Marshall²³, Meghan Frey²³, Jerome Yesavage⁶⁹, Joy L. Taylor⁶⁹, Barton Lane⁶⁹, Allyson Rosen⁶⁹, Jared Tinklenberg⁶⁹, Marwan N. Sabbagh⁷⁰, Christine M. Belden⁷⁰,

Sandra A. Jacobson⁷⁰, Sherye A. Sirrel⁷⁰, Neil Kowall⁷¹, Ronald Killiany⁷¹, Andrew E. Budson⁷¹, Alexander Norbash⁷¹, Patricia Lynn Johnson⁷¹, Thomas O. Obisesan⁷², Saba Wolday⁷², Joanne Allard⁷², Alan Lerner⁷³, Paula Ogorcki⁷³, Leon Hudson⁷³, Evan Fletcher⁷⁴, Owen Carmichael⁷⁴, John Olichney⁷⁴, Charles DeCarli⁷⁴, Smita Kittur⁷⁵, Michael Borrie⁷⁶, T. Y. Lee⁷⁶, Rob Bartha⁷⁶, Sterling Johnson⁷⁷, Sanjay Asthana⁷⁷, Cynthia M. Carlsson⁷⁷, Steven G. Potkin³⁶, Adrian Preda³⁶, Dana Nguyen³⁶, Pierre Tariot³³, Stephanie Reeder³³, Vernice Bates⁷⁸, Horacio Capote⁷⁸, Michelle Rainka⁷⁸, Douglas W. Scharre⁷⁹, Maria Kataki⁷⁹, Anahita Adeli⁷⁹, Earl A. Zimmerman⁸⁰, Dzintra Celmins⁸⁰, Alice D. Brown⁸⁰, Godfrey D. Pearlson⁸¹, Karen Blank⁸¹, Karen Anderson⁸¹, Robert B. Santulli⁸², Tamar J. Kitzmiller⁸², Eben S. Schwartz⁸², Kaycee M. Sink⁸³, Jeff D. Williamson⁸³, Pradeep Garg⁸³, Franklin Watkins⁸³, Brian R. Ott⁸⁴, Henry Querfurth⁸⁴, Geoffrey Tremont⁸⁴, Stephen Salloway⁸⁵, Paul Malloy⁸⁵, Stephen Correia⁸⁵, Howard J. Rosen¹⁶, Bruce L. Miller¹⁶, Jacobo Mintzer⁸⁶, Kenneth Spicer⁸⁶, David Bachman⁸⁶, Elizabeth Finger⁸⁷, Stephen Pasternak⁸⁷, Irina Rachinsky⁸⁷, Dick Drost⁸⁷, Nunzio Pomara⁸⁸, Raymundo Hernando⁸⁸, Antero Sarrael⁸⁸, Susan K. Schultz⁸⁹, Laura L. Boles Ponto⁸⁹, Hyungsub Shim⁸⁹, Karen Elizabeth Smith⁸⁹, Norman Relkin⁹⁰, Gloria Chaing⁹⁰, Lisa Raudin⁹⁰, Amanda Smith⁹¹, Kristin Fargher⁹¹ and Balebail Ashok Raj⁹¹

¹⁶University of California San Francisco, San Francisco, CA, USA. ¹⁷University of California San Diego, San Diego, CA, USA. ¹⁸Mayo Clinic, Rochester, NY, USA. ¹⁹University of California Berkeley, Berkeley, CA, USA. ²⁰University of Pennsylvania, Philadelphia, PA, USA. ²¹University of Southern California, Los Angeles, CA, USA. ²²University of California Davis, Davis, CA, USA. ²³Brigham and Women's Hospital, Harvard Medical School, Boston, MA, USA. ²⁴Indiana University, Bloomington, IN, USA. ²⁵Washington University St. Louis, St. Louis, MO, USA. ²⁶Janssen Alzheimer Immunotherapy, South San Francisco, CA, USA. ²⁷University of Washington, Seattle, WA, USA. ²⁸University of London, London, UK. ²⁹University of Southern California School of Medicine, Los Angeles, CA, USA. ³⁰University of California San Francisco MRI, San Francisco, CA, USA. ³¹University of Michigan, Ann Arbor, MI, USA. ³²University of Utah, Salt Lake City, UT, USA. ³³Banner Alzheimer's Institute, Phoenix, AZ, USA. ³⁴University of Pittsburgh, Pittsburgh, PA, USA. ³⁵University of Pennsylvania School of Medicine, Philadelphia, PA, USA. ³⁶University of California Irvine, Irvine, CA, USA. ³⁷Khachaturian, Radebaugh & Associates, Inc. and Alzheimer's Association's Ronald and Nancy Reagan's Research Institute, Chicago, IL, USA. ³⁸General Electric, Boston, MA, USA. ³⁹Brown University, Providence, RI, USA. ⁴⁰National Institute on Aging/National Institutes of Health, Bethesda, MD, USA. ⁴¹Oregon Health and Science University, Portland, OR, USA. ⁴²Baylor College of Medicine, Houston, TX, USA. ⁴³Columbia University Medical Center, New York, NY, USA. ⁴⁴Washington University, St. Louis, MO, USA. ⁴⁵University of Alabama at Birmingham, Birmingham, MO, USA. ⁴⁶Mount Sinai School of Medicine, New York, NY, USA. ⁴⁷Rush University Medical Center, Chicago, IL, USA. ⁴⁸Wien Center, Vienna, Austria. ⁴⁹Johns Hopkins University, Baltimore, MD, USA. ⁵⁰New York University, New York, NY, USA. ⁵¹Duke University Medical Center, Durham, NC, USA. ⁵²University of Kentucky, Lexington, KY, USA. ⁵³University of Rochester Medical Center, Rochester, NY, USA. ⁵⁴University of California, Irvine, CA, USA. ⁵⁵University of Texas Southwestern Medical School, Dallas, TX, USA. ⁵⁶Emory University, Atlanta, GA, USA. ⁵⁷University of Kansas Medical Center, Lawrence, KS, USA. ⁵⁸University of California, Los Angeles, CA, USA. ⁵⁹Mayo Clinic, Jacksonville, FL, USA. ⁶⁰Yale University School of Medicine, New Haven, CT, USA. ⁶¹McGill University, Montreal Jewish General Hospital, Montreal, Quebec, Canada. ⁶²Sunnybrook Health Sciences, Toronto, Ontario, Canada. ⁶³University of British Columbia Clinic for AD & Related Disorders, Vancouver, British Columbia, Canada. ⁶⁴Cognitive Neurology St. Joseph's, Toronto, Ontario, Canada. ⁶⁵Cleveland Clinic Lou Ruvo Center for Brain Health, Las Vegas, NV, USA. ⁶⁶Northwestern University, Evanston, IL, USA. ⁶⁷Premiere Research Institute Palm Beach Neurology, West Palm Beach, FL, USA. ⁶⁸Georgetown University Medical Center, Washington, DC, USA. ⁶⁹Stanford University, Stanford, CA, USA. ⁷⁰Banner Sun Health Research Institute, Sun City, AZ, USA. ⁷¹Boston University, Boston, MA, USA. ⁷²Howard University, Washington, DC, USA. ⁷³Case Western Reserve University, Cleveland, OH, USA. ⁷⁴University of California Davis Medical Center, Sacramento, CA, USA. ⁷⁵Neurological Care of CNY, New York, NY, USA. ⁷⁶Parkwood Hospital, Parkwood, CA, USA. ⁷⁷University of Wisconsin, Madison, WI, USA. ⁷⁸Dent Neurologic Institute, Amherst, NY, USA. ⁷⁹Ohio State University, Columbus, OH, USA. ⁸⁰Albany Medical College, Albany, NY, USA. ⁸¹Hartford Hospital, Olin Neuropsychiatry Research Center, Hartford, CT, USA. ⁸²Dartmouth Hitchcock Medical Center, Albany, NY, USA. ⁸³Wake Forest University Health Sciences, Winston-Salem, NC, USA. ⁸⁴Rhode Island Hospital, Providence, RI, USA. ⁸⁵Butler Hospital, Providence, RI, USA. ⁸⁶Medical University of South Carolina, Charleston, SC, USA. ⁸⁷St. Joseph's Health Care, Toronto, Ontario, Canada. ⁸⁸Nathan Kline Institute, Orangeburg, SC, USA. ⁸⁹University of Iowa College of Medicine, Iowa City, IA, USA. ⁹⁰Cornell University, Ithaca, NY, USA. ⁹¹University of South Florida Health/Byrd Alzheimer's Institute, Tampa, FL, USA. A full list of members and their affiliations can be found at https://adni.loni.usc.edu/wp-content/uploads/how_to_apply/ADNI_Acknowledgement_List.pdf.

Methods

Unless otherwise noted, all data analysis was conducted, and all figures were created, using Python v.3.7.3, mostly using the numpy, scipy, pandas, scikit-learn, nilearn, matplotlib, seaborn and statsmodels libraries.

Sample characteristics. The total sample for the following analyses consisted of flortaucipir tau PET scans from 1,667 individuals from 5 different cohorts (BioFINDER 1, Seoul, AVID, University of California, San Francisco (UCSF), Alzheimer's Disease Neuroimaging Initiative (ADNI)) and RO948 PET scans from 657 individuals from a sixth cohort (BioFINDER 2). Information pertaining to recruitment, diagnostic criteria and A β positivity assessment for the BioFINDER 1 (ref. ⁴⁷), ADNI⁴⁸, AVID⁴², Seoul⁵⁸, UCSF⁶ and BioFINDER 2 (ref. ²⁸) cohorts have been reported previously. Informed written consent was obtained from all participants or their designated caregiver(s) and all protocols were approved by each cohort's respective institutional ethical review board. Specifically, all BioFINDER participants provided written informed consent to participate in the study according to the Declaration of Helsinki (2013); ethical approval was given by the ethics committee of Lund University and all methods were carried out in accordance with the approved guidelines. Approval for PET imaging was obtained from the Swedish Medicines and Products Agency and the local radiation safety committee at Skåne University Hospital. For UCSF, the study was approved by the University of California (San Francisco and Berkeley) and Lawrence Berkeley National Laboratory institutional review boards for human research. Data from the AVID sample were collected in compliance with the Declaration of Helsinki (2013) and the International Conference on Harmonization guidelines on good clinical practice. Data collection for the Gangnam Severance Hospital sample was approved by the institutional review board of Gangnam Severance Hospital. Information related to participant consent in ADNI can be found at <http://adni.loni.usc.edu>. Some of the data used in the preparation of this article were obtained from the ADNI database (<http://adni.loni.usc.edu>). ADNI was launched in 2003 as a public-private partnership led by principal investigator M. W. Weiner. The primary goal of ADNI has been to test whether serial magnetic resonance imaging (MRI), PET, other biological markers and clinical and neuropsychological assessment can be combined to measure the progression of MCI and early-onset AD. For up-to-date information, see <http://adni.loni.usc.edu>.

From this total sample of 1,667 participants with flortaucipir scans, a subsample was derived including (1) all cognitively unimpaired individuals older than 40 years and (2) individuals who had both a diagnosis of MCI or AD and imaging or fluid evidence of brain A β pathology. All participants with a primary diagnosis other than cognitively unimpaired, which included subjective cognitive decline, MCI or AD were excluded. This subsample, used for all subsequent analysis, consisted of 1,143 individuals. The same screening procedures were used to filter individuals from BioFINDER 2, reducing the samples size from 657 to 469. The characteristics of all samples, including inter-cohort differences, are detailed in Supplementary Table 1.

Image acquisition and preprocessing. Tau PET data acquisition procedures for each cohort have been described previously^{6,27,28,32,46,58}. All tau PET data were processed centrally in Lund by analysts blinded to demographic and clinical data in a manner described previously⁶. Briefly, resampling procedures were used to harmonize image size and voxel dimension across sites. Each image underwent motion correction using the AFNI program 3dvolreg (https://afni.nimh.nih.gov/pub/dist/doc/program_help/3dvolreg.html) and individual PET volumes were averaged within-participant. Next, each participant's mean PET image underwent rigid coregistration to its respective skull-stripped native T1 image and images were intensity-normalized using an inferior cerebellar gray reference region, resulting in standardized update value ratio (SUVR) images. T1 images were processed using FreeSurfer v.6.0 (<https://surfer.nmr.mgh.harvard.edu/>), resulting in native space parcellations of each participant's brain using the Desikan–Killiany (FreeSurfer) atlas. These parcellations were used to extract mean SUVR values within different ROIs for each participant in native space.

SuStaIn. Typical efforts to perform data-driven subtyping of neuroimages in AD are limited by the confound of disease stage. In a sample spanning the AD spectrum from healthy to demented such as ours, disease progression represents the main source of variation in MRI and PET images. Therefore, unless disease stage is somehow accounted for, most clustering algorithms will partition individuals based on their disease stage. This is not useful for parsing heterogeneous patterns related to progression subtypes, which are theoretically orthogonal to disease progression itself. The SuStaIn²³ algorithm surmounts this limitation by combining clustering with disease progression modeling. Detailed formalization of SuStaIn has been published previously²³.

SuStaIn models linear transition across discrete points along a progression of indices of severity (typically z-scores) separately across different ROIs (Supplementary Fig. 1a). Input requires a subject x feature matrix where, in this case, features represent the mean tau PET signal within different ROIs. In addition, 'severity scores', indicating different waypoints along the natural progression of ROI severity, must be provided. Whereas the choice of ROI constrains the spatial dimensions along which individuals may vary, severity scores instead constrain

the temporal dimension of variation. Therefore, the total number of features is represented by the product of m ROIs by n ROI-specific severity scores. Thus, a balance must be struck between resolution in the spatial and temporal dimensions with respect to overall sample size.

Our discovery sample boasted scans from 1,143 individuals, but even given our inclusion criteria, we expected from previous work²⁹ that most individuals (50–60%) will have minimal tau binding (note that SuStaIn will automatically detect these individuals and exclude them from progression modeling). Therefore, we expected the modeling to be performed on a sample of approximately 450–550. Therefore, we decided on 10 different ROIs (spatial features), each with 3 severity scores (temporal dimension), totaling 30 features. Given an arbitrary rule of 10–20 observations per feature, 300–600 observations should provide sufficient power and our sample size should therefore be sufficient.

For the ten spatial features, we opted for left and right lobar ROIs: parietal; frontal; occipital; temporal; and MTL. This choice is justified as follows:

- (1) previous imaging and pathology subtyping studies have revealed variation in AD pathology to often occur within specific lobes, for example, limbic-predominant (MTL), MTL-sparing (parietal), PCA (occipital), logopenic aphasia (temporal) and behavioral variant AD (perhaps frontal)¹⁸; (2) hemispheric laterality in AD is understudied perhaps due to pathological staining often occurring on single hemispheres. However, some laterality has been observed in AD clinical variants (that is, logopenic PPA¹⁵) and may point to differing phenotypes in typical AD; (3) these lobar regions maintain some orthogonality to disease progression since multiple lobes are involved in Braak stages IV–VI⁸.

To define severity score cutoffs, we first sought to normalize SUVR values to account for regional differences in PET signal (due to nonuniformity of off-target binding, perfusion, etc. across the brain)³⁹. Two-component Gaussian mixture models were used to define, for each ROI, a normal (Gaussian-shaped noise) and abnormal distribution. We then created tau z-scores by normalizing all values using the mean of the normal distribution (Extended Data Fig. 1b). This procedure centered the z-score values on the normal distribution to allow for more interpretable values (that is, $z = 2 - 2$ s.d. from normal) and also accounted for region-specific differences in normal and abnormal SUVR distributions. Uniform values of $z = 2, 5$ and 10 were arbitrarily chosen as severity score control points for all ROIs (Extended Data Fig. 1b). However, analyses were also run with alternative z-score values (see the Replication analysis section below).

The number of subtypes (that is, distinct spatiotemporal progressions) was determined through cross-validation. Separately for each $k = 1$ –7 subtypes, tenfold cross-validation was performed where, for each fold, SuStaIn was fitted to 90% of the data and this model was used to evaluate sample likelihood for the 10% left-out participants. For each left-out set, model fit was evaluated using the cross-validation-based information criterion (CVIC; as described in Young et al.²³), as well as out-of-sample log-likelihood. In addition, we used the inner-fold SuStaIn model to assign all outer-fold individuals to a subtype and we evaluated the probability of the maximum likelihood subtype. In theory, a better fit model should produce more high-probability assignments of left-out data, although more subtypes will also make assignment more challenging. k was chosen by evaluating these three metrics in concert (Extended Data Fig. 1c–e). CVIC increased significantly with increasing k , indicating better fit to the data as the number of subtypes increased, although the curve flattened somewhat after $k = 4$ (Extended Data Fig. 1c). Similarly, log-likelihood increased indicating better model fit up until $k = 4$, after which no improvement was seen (Extended Data Fig. 1d). In contrast to these fit statistics, cross-validated maximum likelihood subtype probability decreased with increasing k , indicating less confident assignment of left-out data with more subtypes. This decline was steady, although the median probability dropped below 0.5 after $k = 4$. Taken together, $k = 4$ appeared to be the best solution to maximize model fit but minimize detriment to subtype confidence. We also noted that no subtypes after $k = 4$ had more than one 'parent' subtype. In other words, solutions 3 and 4 featured subtypes that were composed of multiple parent subtypes, whereas all solutions thereafter featured only subtypes that split off from a single parent subtype. This could be indicative of a certain level of hierarchical convergence at $k = 4$ (Extended Data Fig. 1f).

Finally, SuStaIn was run on the whole sample with the selected $k = 4$. Note that for model fitting, SuStaIn uses a uniform prior on disease subtype and stage (that is, it assumes all subtype and stage combinations equally likely). Note also that the model is initialized with an expectation–maximization algorithm and therefore does not require a burn-in period⁴³. The model uncertainty was estimated using 10,000 Markov chain Monte Carlo iterations. SuStaIn calculates the probability that each individual falls into each stage of each subtype and individuals are assigned to their maximum likelihood subtype and stage. Note that individuals who do not express abnormal tau in any region are classified by SuStaIn as 'stage 0' and are not assigned to a subtype. The proportion of individuals classified into each subtype was quantified. We also stratified this quantification by clinical diagnosis and by cohort to assess the frequency of subtypes in each contributing dataset. Finally, we quantified the proportion of participants who did not fall well into any subtype (no subtype probability $>50\%$).

Post hoc subtype correction. Manual inspection of subtype progressions suggested that the early stages of one subtype (S2: MTL-sparing; Results) were

composed mostly of individuals who were CN with abnormally high tau PET binding throughout the cortex but little-to-no tau in typical early-mid AD regions, that is, false (tau) positives. Specifically, these individuals showed elevated binding throughout the cortex, including sensorimotor and frontal regions (regions where tau typically accumulates only in the latest stages of AD⁸) but had low tau levels in the temporal lobes (Extended Data Fig. 1a). On an individual basis, such individuals showed a tau PET signal that was slightly but globally elevated, with several small 'hotspots' distributed diffusely throughout the frontal, parietal and occipital cortex. While it is unclear whether this elevated binding represents off-target binding, diffuse low-level target binding or other methodological issues, consensus among coauthors was that these individuals were not consistent with an AD phenotype. We used Gaussian mixture modeling across all individuals as described in Vogel et al.²⁹ to define the probability of abnormal tau positivity in each of the left and right entorhinal cortex and precuneus, respectively. We then marked individuals who had <90% probability of tau in all four regions as low-probability tau individuals (T–). These individuals also underwent manual inspection. Next, we identified T– individuals in the MTL-sparing subtype, finding that 40.6% of this subtype was composed of this group and all were classified as stage 5 (of 31) or below. Furthermore, these individuals showed many other indications of being false (tau) positives: they had normal MMSE scores, were older, less likely to be Aβ+ and less likely to be MCI or AD (Extended Data Fig. 2b,c). We assumed SuStaIn appended this specific group of T– individuals to the MTL-sparing subtype because the individuals (1) had abnormally high tau in at least one ROI as per our calculations (even if that abnormal signal was not driven by pathology); (2) the abnormal tau was located mainly in the isocortex inclusive of the parietal lobe; and (3) these individuals did not have elevated MTL binding. Since SuStaIn is an unsupervised algorithm, the pathological MTL-sparing phenotype became conflated with this specific profile of T– individuals. To correct this issue, we converted all T– individuals classified as MTL-sparing to subtype 0 for all further analysis.

Visualization of subtype-specific tau PET patterns. To visualize the tau PET patterns for each subtype, we calculated the mean tau z-score for each Desikan-Killiany (FreeSurfer) atlas ROI. To visualize the progression of the subtype pattern across SuStaIn stages, for each subtype, we created mean images for all individuals falling into the following SuStaIn stage bins: 2–6; 7–11; 12–16; 17–21; and 22–26. To deduce regions with relatively greater or less tau signal for each subtype, we created region-wise one-versus-all ordinary least squares (OLS) linear models comparing regional tau in one subtype to all others. This analysis was performed to visualize subtype models inferred by SuStaIn using individual data and explore differences between subtypes. Each model included ROI tau z-scores as the dependent variable, a one-hot dummy variable representing membership in the reference subtype and SuStaIn stage as a covariate. These models were false discovery rate (FDR)-corrected for the number of comparisons (that is, number of ROIs).

Subtype characterization. Several demographic, cognitive and genetic variables were available for nearly all individuals across the five cohorts in our main (discovery) cohort. These variables included clinical diagnosis (100%), age (99.8%), sex (100%), years of education (97.1%), MMSE score (97.7%) and APOE4 allele carriage (89.5%). Only the UCSF sample provided diagnoses of clinical AD variants such as PCA¹⁶ and logopenic PPA¹⁷. In addition, most individuals underwent extensive cohort-specific cognitive batteries assessing multiple domains of cognition. To utilize this rich cognitive data, we created cognitive domain scores separately within each cohort by taking the mean of several z-scored tests within the following cognitive domains: memory; executive function; language; and visuospatial function. Supplementary Table 5 indicates which cognitive tests were used in each cognitive domain score across each cohort. We calculated global cognition as the mean between the four domain scores. Finally, we additionally regressed global cognition out of each domain score to create 'relative' cognitive domain scores. These scores are useful for assessing the degree of domain-specific impairment above and beyond global impairment. The various absolute and relative domain scores were then aggregated across all cohorts to maximize the sample size available for cognitive tests: memory (86.6%); language (81.3%); executive function (85.5%); and visuospatial function (82.0%). While aggregating scores of different compositions across cohorts of different compositions presents a suboptimal solution, we rest on sample sizes and statistical correction helping to overcome these limitations.

Subtypes were statistically compared to one another and to tau– (that is, stage 0) individuals to determine subtype-specific characteristics. These analyses compared age, sex, education, APOE4 carriage, MMSE, global cognition, total tau and total tau asymmetry. Comparisons between subtypes and stage 0 individuals additionally included the four cognitive domain scores, while comparison between subtypes instead included the four 'relative' cognitive domain scores. This statistical comparison involved three steps: (1) comparison to tau– individuals: tau– individuals were those characterized as 'subtype 0' by SuStaIn, that is, those individuals who did not demonstrate any abnormal tau events. An OLS linear model was fitted with each variable described above as the dependent variable and with dummy-coded subtype entered as the independent variable (with S0 as

the reference subtype). The model also included age, sex, education, clinical status (CN, MCI, AD) and cohort as covariates (except when that covariate was the dependent variable). Model *t* and *P* values were stored for each model and the latter were FDR-corrected; (2) comparison between subtypes. A one-versus-all approach was applied to subtyped individuals only to assess how different tau progression subtypes differed from one another. Separately for each subtype, models were fitted for each variable with a single dummy variable entered indicating membership to that subtype. Models once again covaried for age, sex, education, clinical status (CN, MCI, AD), cohort and, this time, SuStaIn stage. *T* and *P* values were stored and the latter were FDR-corrected for the number of variables assessed; (3) finally, each subtype was compared directly to each other subtype (that is, one-versus-one comparison). OLS models were fitted with dummy-coded subtype variables as the dependent variable, cycling each subtype as the reference subtype. *T* and *P* values for each of these models were stored and the latter were FDR-corrected for the number of comparisons (that is, the number of dependent variables). These models were also adjusted for age, sex, education, clinical status (CN, MCI, AD), cohort and SuStaIn stage. For space reasons, the results of (3) are only visible in Extended Data Fig. 8.

All models were subjected to diagnostics to ensure our data fulfilled the assumptions of the OLS regression models. We found the residuals of all models to be normally distributed (Anderson–Darling tests *P*>0.05). Furthermore, we found no strong evidence for autocorrelation (Durbin–Watson test, 1.5 < all models < 2.5), outliers (Cook's distance of all participants <0.5), multicollinearity (variance inflation factor for all covariates <100; besides age (23–27), sex (8–12) and education (13–17), all variance inflation factor <10) or heteroscedasticity (visual assessment of distribution around the mean of residuals) in any of our models.

We also assessed the relationship between SuStaIn stage and two variables: age and MMSE. For these analyses, stage was correlated with age and MMSE and the results were visualized across the whole sample and stratified by subtype. As a post hoc analysis, we separated individuals into different age groups: 65 or younger and older than 65. We then reassessed age by SuStaIn stage correlations within each of these age groups.

Longitudinal MMSE data were also available for individuals from all cohorts, totaling 735 individuals with at least 2 time points; 195 individuals had an additional third time point, 29 had a fourth and 3 had a fifth. The mean latest follow-up was 1.72 years from PET scan (s.d.=0.64). Linear mixed-effect models were used to assess the difference in longitudinal MMSE change between subtypes. All models were fitted using the lme4 library in R (v4.0.3), using type III sum of squares, unstructured covariance matrices and Satterthwaite approximation to calculate the denominator degrees of freedom for *P* values. Models featured MMSE measurements as the dependent variable, interactions between time from baseline and dummy-coded subtype variables as the independent variables of interest (cycling the reference subtype), subject ID as a random effect (allowing for random intercepts and slopes) and age, sex, education, cohort, dummy-coded variables for MCI and AD and SuStaIn stage as covariates of no interest. One-versus-all models were also fitted for each participant using dummy-coded subtype variables and significant effects were reported. We additionally repeated the one-versus-all subtype models within each cohort separately and used this to calculate a meta-analysis by finding a weighted mean of the *t* values and s.e.m. Since this analysis was confirmatory, we used a one-tailed significance test to calculate the *P* values.

Replication analysis. We performed two types of replication analysis. To ensure that our results were not driven by arbitrary *z*-score cutoffs, we reran models with completely different cutoffs. To ensure the results were not driven by our sample or unique to the flortaucipir radiotracer, we repeated the analysis de novo in a separate cohort using a different tau PET radiotracer.

SuStaIn require *z*-score values to anchor the pseudotime for each ROI (Subtype and stage inference section) and we chose values of 2, 5 and 10 for all ROIs so as not to let any region bias or influence the model unduly and to aid comparability across different regions. To ensure our results were not driven by this choice, we reran the model with a different set of *z*-score values chosen in a data-driven manner. The object was to allow the distribution of tau PET data in each region to define natural waypoints in the data. For each input region, we fitted Gaussian mixture models to the data, varying the number of components between 1 and 5. We used the model fit (Akaike information criterion) to decide the optimal number of components for each region. Finally, we used fivefold cross-validation to determine the boundaries of these Gaussians to define anchors for each regions. We did this separately for each ROI; as a result, different ROIs had different waypoints and even different numbers of waypoints (Supplementary Table 6). We then refitted the SuStaIn model to the data and compared the results to the original model using spatial correlation (see below).

While the five cohorts from the main discovery sample all use flortaucipir as the tau PET tracer, a sixth cohort (BioFINDER 2) was available that instead used the RO948 radiotracer. While the two tracers have similar binding patterns, RO948 tends to have less off-target binding in the basal ganglia and better MTL signal but frequently boasts a high meningeal signal that can affect cortical SUVR measurement⁵³. Because of these differences, we opted to leave BioFINDER 2 out

of the discovery sample and instead use it as a replication cohort. This strategy allowed us not only to evaluate the stability of the subtypes in a new cohort, but also allowed us to evaluate whether the subtypes were robust to the tau PET radiotracer.

We reran SuStaIn de novo in the BioFINDER 2 sample using identical procedures to those described above (Subtype and stage inference section), although using the discovery sample to inform the number of subtypes. The resulting subtypes were visualized and assessed quantitatively using spatial correlations. Specifically, mean within-subtype SUVRs were computed for each (FreeSurfer) ROI and each discovery subtype ROI vector was correlated to each replication (BioFINDER 2) subtype ROI vector. To account for whether different sample sizes contributed to differing results between the discovery and replication datasets, we performed a split-half analysis with the discovery sample. Specifically, we split the discovery sample in half and ran SuStaIn separately on each half, once again using the original discovery sample to inform the number of subtypes. We then compared each half, which had a sample size comparable to that of BioFINDER 2, to the BioFINDER 2 samples using spatial correlations.

Assessment of longitudinal stability. Longitudinal PET data were available for individuals across all cohorts except for the UCSF cohort, totaling 519 individuals with at least 2 time points (mean follow-up time = 1.42 years, s.d. = 0.58). These longitudinal scans were used to validate the stability of subtypes over time under the hypothesis that individuals should remain the same subtype but should advance (or remain stable) in SuStaIn stage over time. ROIs for the longitudinal datasets were z-scored as described above but using the cross-sectional cohort as the cohort for normalization. The SuStaIn model fitted to the cross-sectional dataset was used to infer subtype and stage of longitudinal data (all time points). Confusion matrices were built to assess subtype stability between baseline and first follow-up. Stability was calculated as the proportion of individuals classified as the same subtype at follow-up or who advanced from stage 0 into a subtype, compared to the total number of individuals. Stability was also calculated excluding individuals who were classified as stage 0 at baseline or follow-up. We also assessed the influence of subtype probability (that is, the probability an individual falls into their given subtype) on individual subtype stability. Specifically, we compared the subtype probability of stable to unstable individuals with a *t*-test. We additionally calculated overall model stability after excluding individuals using various subtype probability thresholds.

Subtype progression was assessed by observing change in SuStaIn stage over time in stable subtype individuals. We calculated the proportion of individuals who advanced, were stable or regressed in disease stage over time before and after accounting for model uncertainty. Specifically, while stages are generally characterized by advancing abnormality in a given region, uncertainty leads to some stages being characterized by probabilities of progressing abnormalities in more than one region. Therefore, individuals who advanced or regressed to a stage with event probabilities overlapping with their previous stage were considered stable. We also calculated annual change in SuStaIn stage by dividing total change in SuStaIn stage by the number of years between baseline and final available time point. We used a one-sample *t*-test against zero to assess whether significant change over time was observed across the whole sample and within each subtype. We used analysis of variance and Tukey's post hoc tests to assess differences in annual change in stage across the different subtypes. We also correlated annual change in stage with baseline stage and with age.

Individual forecasting of longitudinal tau progression. SuStaIn models spatiotemporal subtype progressions but does so using only cross-sectional data. Therefore, longitudinal data can be used as 'unseen' or 'left-out' data, which can be used to test whether and to what extent individuals follow the trajectories predicted by SuStaIn. We accomplished this by using an individual's subtype and stage probability to generate a predicted second time point and comparing the change between baseline and predicted follow-up to change between baseline and actual follow-up.

To do this, we first sought to predict the rate of change of stage for each individual. We trained a Lasso model to predict individual annualized change in SuStaIn stage (Δ stage) using the available data and cross-validation to get out-of-sample predictions for each individual. Features included age, sex, education, amyloid status, APOE4 status, baseline stage MMSE and dummy-coded variables for MCI, AD and each subtype. For each fold, the model was trained on 90% of the data and this model was used to predict Δ stage in the 10% left-out individuals. This process was repeated until predictions were made for each individual. The mean absolute error between the predicted and true Δ stage was 0.91 stages per year. The predicted Δ stage was used for subsequent aspects of the tau prediction. This is important because we are minimizing the amount of longitudinal information leaking into the forecast.

Using this predicted Δ stage, we were then able to predict an individual's stage at follow-up $k_{i,\text{new}}$ given any stage at baseline k , as $k_{i,\text{new}} = k + \Delta_{\text{stage}} t_i$, where t_i is the time between follow-up visits in years.

We can then evaluate the SuStaIn-predicted pattern of regional tau deposition at baseline Y_{ij} as:

$$Y_{ij} = \sum_{c=1}^C \sum_{k=0}^K A_{j,c,k} P_{i,c,k}$$

or at follow-up z_{ij} as:

$$Z_{ij} = \sum_{c=1}^C \sum_{k=0}^K A_{j,c,k_{i,\text{new}}} P_{i,c,k}$$

where $A_{j,c,k}$ is an 'archetype' indicating the expected amount of tau deposition for biomarker j at stage k of subtype c and $P_{i,c,k}$ is the probability subject i is at stage k of subtype c . The archetype $A_{j,c,k}$ is estimated probabilistically from the Markov chain Monte Carlo samples of uncertainty provided by the SuStaIn algorithm, giving an average archetypal pattern accounting for the uncertainty in the progression pattern of each subtype. This means that each SuStaIn-predicted pattern Y_{ij} accounts for both uncertainty in the progression pattern of each subtype as well as uncertainty in the subtype and stage of each individual.

Therefore, we can represent the predicted change in tau as $Z_{ij} - Y_{ij}$. This vector represents the predicted change in tau z-score in each of the ten spatial input features to SuStaIn (that is, left and right temporal, parietal, occipital, frontal and medial temporal lobes). We evaluated the prediction by computing, for each individual, the correlation between the predicted and true regional tau change vectors. We evaluated the overall prediction across the whole sample, and within subtypes, by comparing the average prediction against chance using one-sample *t*-tests against a correlation of zero.

Epidemic spreading model. Perhaps the most prominent hypothesis of tau spread suggests tau oligomers spread directly from neuron to neuron through axonal connections. Under this hypothesis, diverse but systematic variations in tau spreading may be driven by variability in macroscale connectivity, network organization or vulnerable circuits. We tested this idea by investigating whether a network diffusion model simulating tau spread through the human connectome could recapitulate the various subtype patterns discovered by SuStaIn. We have previously applied the epidemic spreading model (ESM)⁵⁹ to tau PET data, showing how diffusion of an agent through human connectivity data (measured with diffusion imaging-based tractography) can explain a majority of the variance of spatial tau patterns across a population of individuals along the AD spectrum²⁹. In this study, we conducted the exact same analysis separately for each subtype identified through SuStaIn. We further allowed the ESM to identify regional epicenters separately for each subtype under the hypothesis that different subtype patterns may be driven by prominence of different corticolimbic networks.

As described in Vogel et al.²⁹, each tau PET ROI was converted to tau⁺ probabilities using mixture modeling. This process is similar to the z-scoring procedure (Extended Data Fig. 1), although in this case, the probability that values fall onto the abnormal distribution is ascertained using fivefold cross-validation. These measures represent the probability that a given ROI exhibits tau in the abnormal range. Connectivity was measured from a dataset of 60 young healthy individuals from the CMU-60 DSI template (<https://www.cmu.edu/dietrich/psychology/cognitiveaxon>). Deterministic tractography was calculated for each individual by finding connections between ROIs using orientation distribution functions; connectivity was measured using the anatomical connection density metric⁵⁹. Images were assessed for quality and connectomes were averaged across all 60 individuals. For each subtype separately, the ESM was fitted across all individuals, cycling through the average of each left-right pair of cortical ROIs (including the hippocampus and amygdala, 33 pairs in total) as the model epicenter. The best-fitting epicenter was selected by finding the model with the minimum mean Euclidean distance between model-predicted and model-observed tau spatial pattern across individuals. Model accuracy was represented as the r^2 between the mean observed ROI-level tau PET probabilities and mean predicted probabilities across individuals. For each subtype, we compared the r^2 of the model using the best-fitting epicenter to the r^2 of models using an entorhinal epicenter. To gain confidence in the individual-specific epicenter, we bootstrapped the sample 1,000 times and recomputed the best-fitting epicenter for each subtype. Epicenter probability was calculated as the frequency that an epicenter was selected as the best epicenter across bootstrap samples.

We were additionally interested in how secondary seeding evolved over the course of each subtype progression. While the ESM is designed to ascertain the true pathological epicenter, the selected epicenter reflects the seeding point that best matches the spatial pattern of the dependent variable. As such, it is likely that 'secondary epicenters' become important for disease spread at later disease stages. We binned individuals for each subtype into disease stage bins, as with Fig. 1e. Individual epicenters were ascertained for each subject and were aggregated based on lobe (MTL, temporal, frontal, parietal, occipital). We then calculated epicenter frequency among individuals in each stage bin for each subtype. This allowed us to track how the secondary epicenter evolved throughout the disease course for each subtype trajectory.

We repeated this same analysis with a different connectome based on resting state functional MRI connectivity from an elderly population and using a higher-resolution atlas. The sample consisted of resting state functional MRI

scans from 422 healthy older controls (166 A β^+), 138 individuals with subjective cognitive decline but without objective impairment (48 A β^+) and 83 A β^+ MCI patients; 57 individuals overlapped between this sample and the tau PET discovery sample used for analysis. Functional data were processed using the modified CPAC pipeline⁶⁰ involving slice time correction, bandpass filtering at 0.01–0.1 Hz, regression of motion, white matter and cerebrospinal fluid signal, CompCor physiological noise and the 24 Friston parameters. The time series also underwent adaptive censoring of volumes for which DVARS jumps above the median + 1.5 \times interquartile range were observed. Time series were averaged within ROIs of the 246-ROI Brainnetome cortical/subcortical atlas (<https://atlas.brainnetome.org/>), nodewise connectivity was calculated using either Fisher's z-transformed correlations or partial correlation. The ESM was fitted using the bilateral A35/36 ROI as the model epicenter and the following combinations of parameters were varied: regions (cortical only or all regions); subject-base (A β^+ only versus all individuals); density (edgewise thresholding at 0.02, 0.5, 0.1, 0.25 and 1 or partial correlation with no thresholding); and normalization (whether connectivity matrices were normalized after density thresholding). The only parameter strongly affecting model performance was density threshold—partial correlation far outperformed all other conditions. Using all regions over only cortical regions bore slight advantages as did using all individuals over only A β^+ . Normalization had no effect on outcomes. The best-fitting model was used for further analysis. The ESM was fitted to each individual separately and epicenter bootstrapping was performed, both as described above.

Reporting Summary. Further information on research design is available in the Nature Research Reporting Summary linked to this article.

Data availability

The tau PET data contributing to this study were sourced from six different cohorts. One of them, ADNI, is a public access dataset and can be obtained by application from <http://adni.loni.usc.edu/>. Data from the other datasets are not publicly available for download, but access requests can be made to the respective study investigators: BioFINDER 1,2—O.H.; UCSF Memory and Aging Center—G.D.R.; Gangnam Severance Hospital—C.H.L.; AVID Radiopharmaceuticals—M.J.P. and M.D.D. Additionally, the CMU-60 diffusion tensor imaging (DTI) data used to create the template DTI connectomes are publicly available and can be accessed at <https://www.cmu.edu/dietrich/psychology/cognitiveaxon/data.html>.

Code availability

Python and MATLAB implementations of the SuStaIn algorithm are available on the UCL-POND GitHub page: <https://github.com/ucl-pond>. The ESM algorithm is available for academics as part of open-access, user-friendly software (for further details, visit <https://www.neuropm-lab.com/>).

References

58. Cho, H. et al. Predicted sequence of cortical tau and amyloid- β deposition in Alzheimer disease spectrum. *Neurobiol. Aging* **68**, 76–84 (2018).
59. Iturria-Medina, Y., Sotero, R. C., Toussaint, P. J. & Evans, A. C. Epidemic spreading model to characterize misfolded proteins propagation in aging and associated neurodegenerative disorders. *PLoS Comput. Biol.* **10**, e1003956 (2014).
60. Craddock, C. et al. Towards automated analysis of connectomes: the configurable pipeline for the analysis of connectomes (C-PAC). *Front. Neuroinform.* <https://doi.org/10.3389/conf.fninf.2014.08.00117> (2013).

Acknowledgements

The authors thank M. Chakravarty, B. Misic, P. Bellec, P. Rosa-Neto, A. Dagher, E. Hamel and W. Seeley for feedback during the composition of this manuscript. J.W.V. acknowledges support from the government of Canada through a tri-council Vanier Canada Graduate Doctoral fellowship from the McGill Centre for Integrative Neuroscience and the Healthy Brains, Healthy Lives initiative, and from the National Institutes of Health (NIH) (no. T32MH019112). A.L.Y. is supported by a Medical Research Council Skills Development Fellowship (MR/T027800/1). N.P.O. is a UK Research and Innovation Future Leaders Fellow (no. MR/S03546X/1). N.P.O. and D.C.A. acknowledge support from the UK National Institute for Health Research University College London Hospitals Biomedical Research Centre, and D.C.A. acknowledges support from the Engineering and Physical Sciences Research Council grant no. EP/M020533/1. M.J.G. is supported by the Miguel Servet program (no. CP19/00031) and a research grant (no. PI20/00613) of the Instituto de Salud Carlos III-Fondo Europeo de Desarrollo Regional. R.L.J. acknowledges support from the NIH (no. K99AG065501). This project received funding from the European Union's Horizon 2020 research and innovation programme under grant no. 666992. The BioFINDER studies are supported

by the Swedish Research Council (no. 2016-00906), the Knut and Alice Wallenberg Foundation (no. 2017-0383), the Marianne and Marcus Wallenberg Foundation (no. 2015.0125), the Strategic Research Area MultiPark (Multidisciplinary Research in Parkinson's disease) at Lund University, the Swedish Alzheimer's Foundation (no. AF-939932), the Swedish Brain Foundation (no. FO2019-0326), the Swedish Parkinson Foundation (no. 1280/20), the Skåne University Hospital Foundation (no. 2020-O000028), Regionalt Forskningsstöd (no. 2020-0314) and the Swedish Federal Government under the ALF agreement (no. 2018-Projekt0279). The Tau PET study in Gangnam Severance Hospital was supported by a grant from the Basic Science Research Program through the National Research Foundation of Korea funded by the Ministry of Education (nos. NRF2018R1D1A1B07049386 and NRF2020R1F1A1076154) and a grant from the Korea Health Technology R&D Project through the Korea Health Industry Development Institute funded by the Ministry of Health and Welfare, Republic of Korea (grant no. HI18C1159). We also thank B. L. Miller, H. J. Rosen, M. Gorno Tempini and W. Jagust for supporting the UCSF tau-PET studies, which were funded through the following sources: National Institute on Aging (NIA) no. R01 AG045611 (G.D.R.), no. P50 AG23501 (B.L.M., H.J.R., G.D.R.), no. P01 AG019724 (B.L.M., H.J.R., G.D.R.). The precursor of ¹⁸F-flortaucipip was provided by AVID Radiopharmaceuticals. The precursor of ¹⁸F-flutemetamol was sponsored by GE Healthcare. The precursor of ¹⁸F-RO948 was provided by Roche. Data collection and sharing for this project were funded by ADNI (NIH grant no. U01 AG024904) and Department of Defense ADNI (award no. W81XWH-12-2-0012). ADNI is funded by the NIA, the National Institute of Biomedical Imaging and Bioengineering and through generous contributions from the following: AbbVie, Alzheimer's Association; Alzheimer's Drug Discovery Foundation; Araclon Biotech; Bioclinica; Biogen; Bristol Myers Squibb; CereSpir; Cogstate; Eisai; Elan Pharmaceuticals; Eli Lilly and Company; EUROIMMUN; F Hoffmann-La Roche and its affiliated company Genentech; Fujirebio; GE Healthcare; IXICO; Janssen Alzheimer Immunotherapy Research Development; Johnson & Johnson Pharmaceutical Research Development; Lumosity; Lundbeck; Merck; Meso Scale Diagnostics; NeuroRx Research; Neurotrack Technologies; Novartis Pharmaceuticals Corporation; Pfizer; Piramal Imaging; Servier; Takeda Pharmaceutical Company; and Transition Therapeutics. The Canadian Institutes of Health Research is providing funds to support ADNI clinical sites in Canada. Private sector contributions are facilitated by the Foundation for the National Institutes of Health (www.nih.gov). The grantee organization is the Northern California Institute for Research and Education, and the study is coordinated by the Alzheimer's Therapeutic Research Institute at the University of Southern California. ADNI data are disseminated by the Laboratory for Neuro Imaging at the University of Southern California. Finally, we thank all participants of this study and the families and caregivers of the patients included for their support in volunteering data for this study. Data used in the preparation of this article were obtained from the Alzheimer's Disease Neuroimaging Initiative (ADNI) database (<http://adni.loni.usc.edu/>). As such, the investigators within the ADNI contributed to the design and implementation of ADNI and/or provided data but did not participate in analysis or writing of this report.

Author contributions

J.W.V., O.H. and A.C.E. conceptualized the work. J.W.V., A.L.Y., N.P.O., L.M.A., M.J.P., M.J.G and O.H. contributed to the analytical design. M.J.P., M.D.D., G.D.R., C.H.L. and O.H. acquired and provided the data. R.S., R.O., O.T.S. and R.L.J. contributed to data curation and processing. J.W.V. analyzed the data. A.L.Y. and D.C.A. originally created the SuStaIn algorithm, and N.P.O. and L.M.A. contributed to its execution. Y.I.M. created the ESM algorithm. J.W.V. and O.H. drafted the manuscript. All authors interpreted the data and contributed substantively to revising the manuscript.

Competing interests

M.J.P. and M.D.D. are employees of AVID Radiopharmaceuticals, a wholly owned subsidiary of Eli Lilly and Company, and are minor stockholders in Eli Lilly and Company. O.H. has acquired research support (for the institution) from AVID Radiopharmaceuticals, Biogen, Eli Lilly and Company, Eisai, GE Healthcare, Pfizer and Roche. In the past two years, he has received consultancy/speaker fees from AC Immune, ALZpath, Biogen, Cerveau and Roche. The remaining authors declare no competing interests.

Additional information

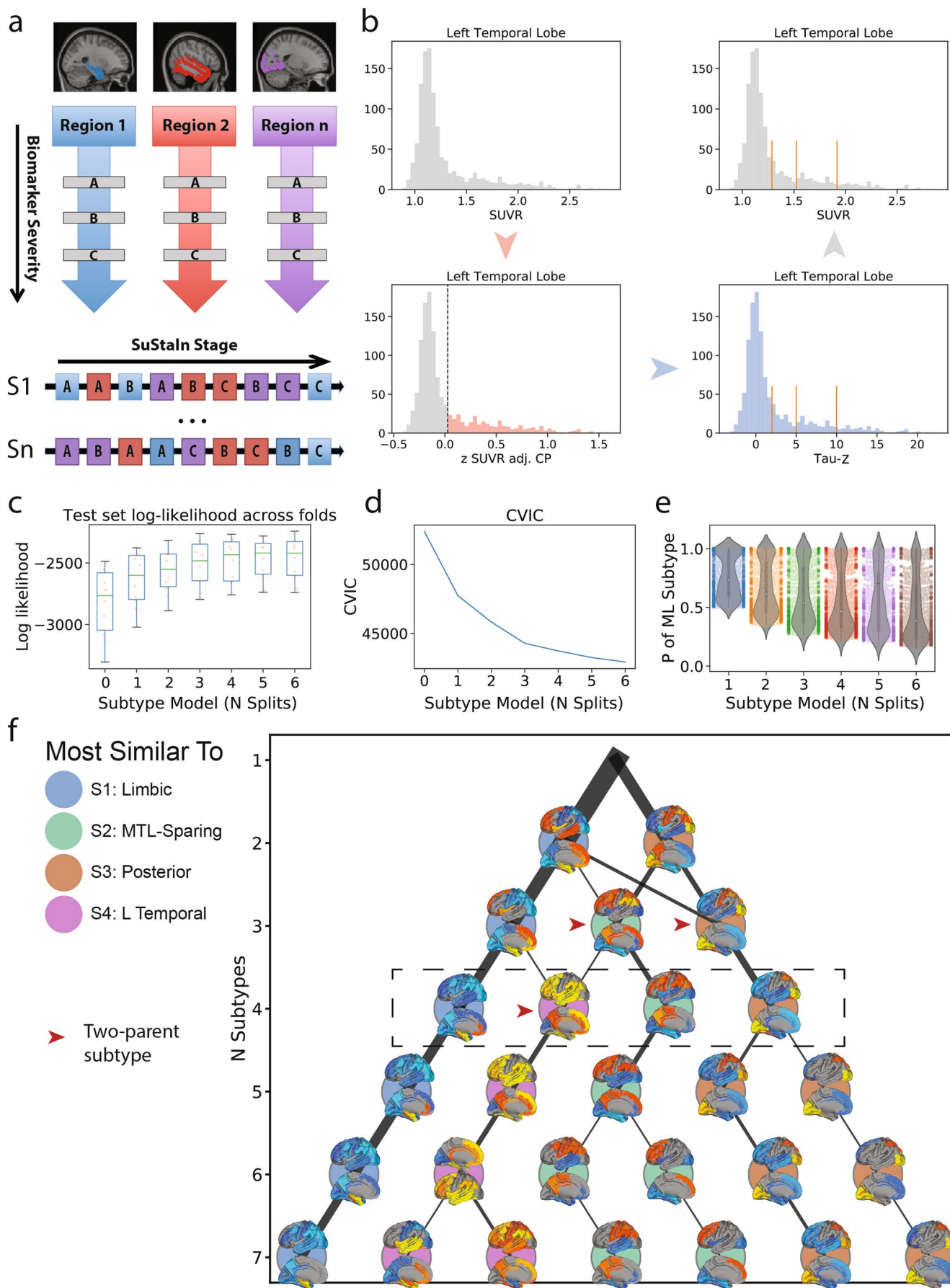
Extended data is available for this paper at <https://doi.org/10.1038/s41591-021-01309-6>.

Supplementary information The online version contains supplementary material available at <https://doi.org/10.1038/s41591-021-01309-6>.

Correspondence and requests for materials should be addressed to J.W.V. or O.H.

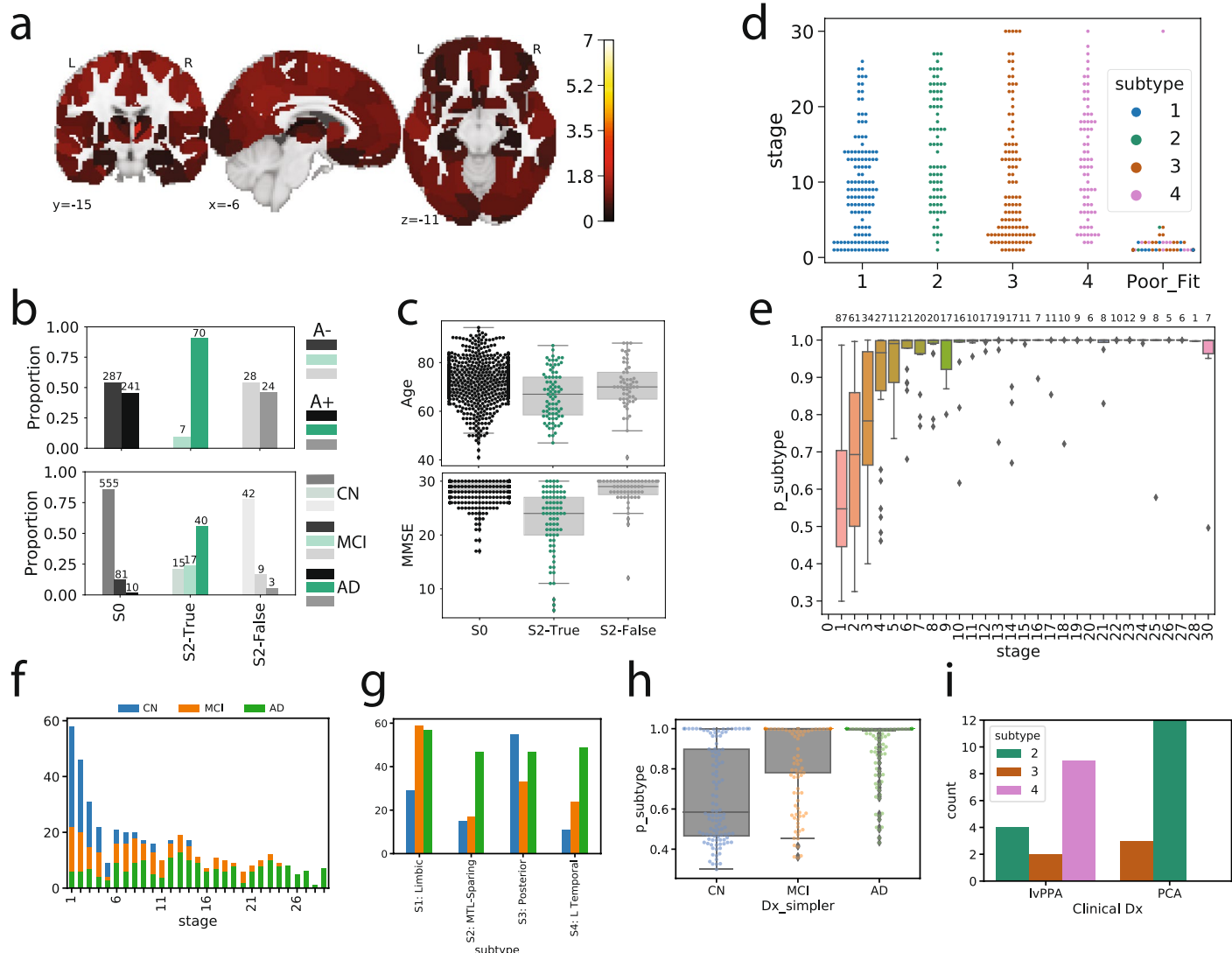
Reprints and permissions information is available at www.nature.com/reprints.

Peer reviewer information *Nature Medicine* thanks Giovanni Frisoni and the other, anonymous, reviewer(s), for their contribution to the peer review of this work. Jerome Staal was the primary editor on this article and managed its editorial process and peer review in collaboration with the rest of the editorial team.

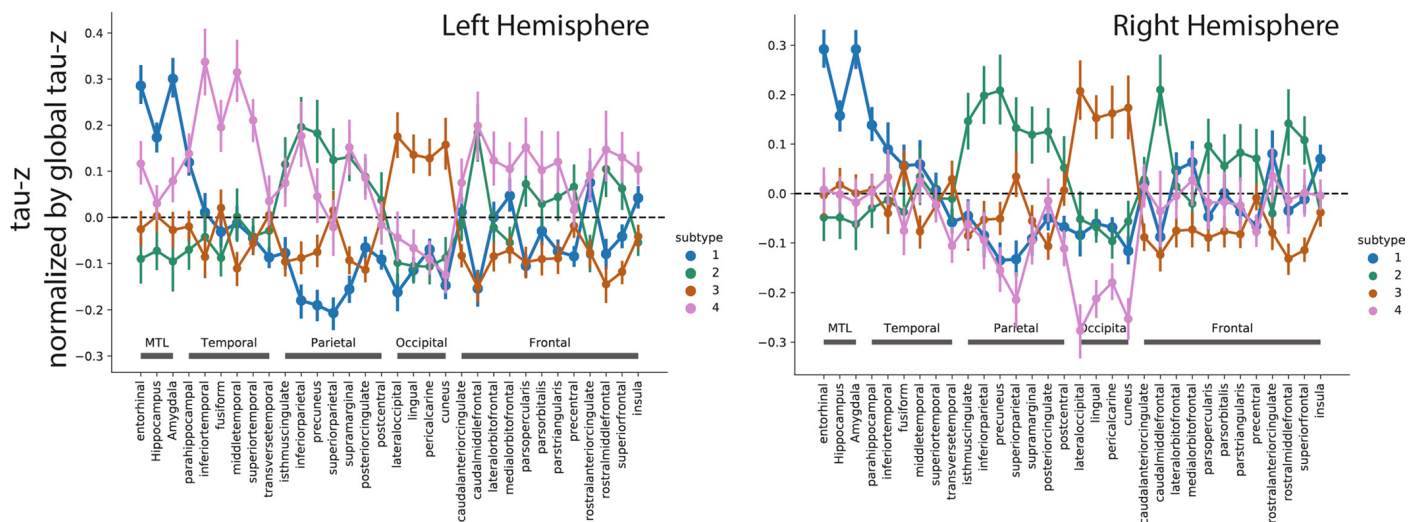


Extended Data Fig. 1 | See next page for caption.

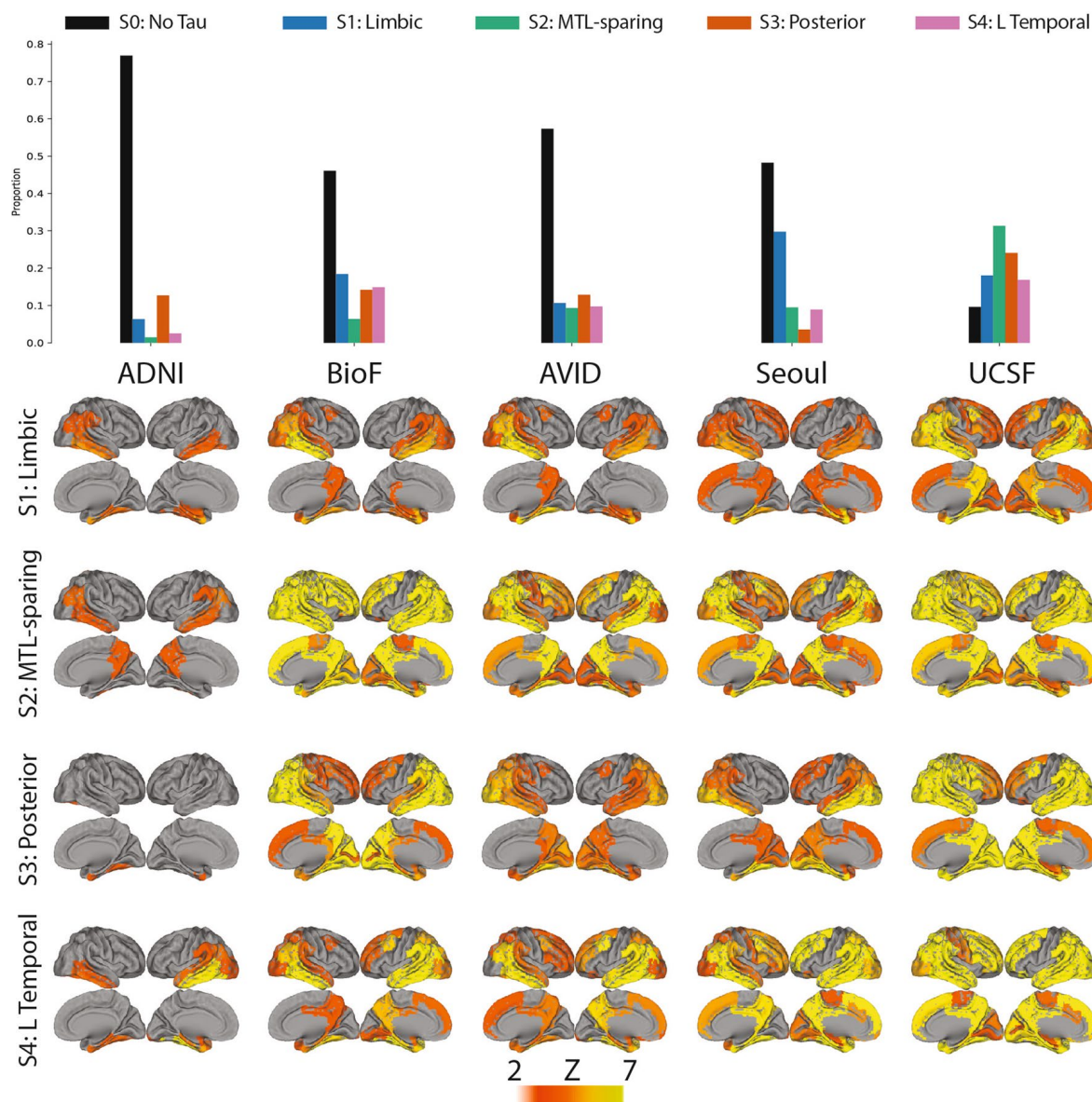
Extended Data Fig. 1 | Methodological details. Methodological details. **a**, SuStaln requires both spatial (for example brain regions) and pseudotemporal (for example Z-score waypoints representing advancing biomarker severity) features as input. SuStaln models linear change between waypoints across multiple biomarkers and uses clustering to fit subtype trajectories representing distinct biomarker sequences. **b**, Each spatial feature was z-scored in order to derive interpretable waypoints. Example: (top left), SUVR distribution in the left temporal lobe. (bottom-left) Distribution of standardized residuals after regression of choroid plexus. Gaussian mixture-modeling identifies 'normal' (grey) and 'abnormal' (red) tau-PET values within this distribution. (bottom right) Mean and SD of 'normal' distribution used to normalize the whole distribution, creating 'Tau Z-scores'. Tau Z-scores of 2, 5 and 10 are used as waypoints. (top-right) Tau-z scores superimposed onto the original SUVR distribution. For each subtype model ($k=1-7$), **c**) distribution of average negative log-likelihood, **d**) CVIC, and **e**) distribution of the probability of the maximum-likelihood subtype across cross-validation folds of left-out individuals. Higher log-likelihood, lower CVIC represents better model fit. **f**, Visualization of subtype solutions $k=2-7$. For each subtype, the rendered brains show significant regional tau difference between the subtype and all other subtypes in its solution. Connecting-line thickness indicates how many subjects are shared between a subtype and each subtype from its parent and child solutions. Circle color represents which $k=4$ subtypes (outlined in the dashed box) each subtype is most similar to, in terms of the number of overlapping subjects. Red arrowheads indicate subtypes that were formed by pooling individuals from two different parent subtypes. For boxplots in c,e, center line=median, box=inner quartiles, whiskers=extent of data distribution except *=outliers.



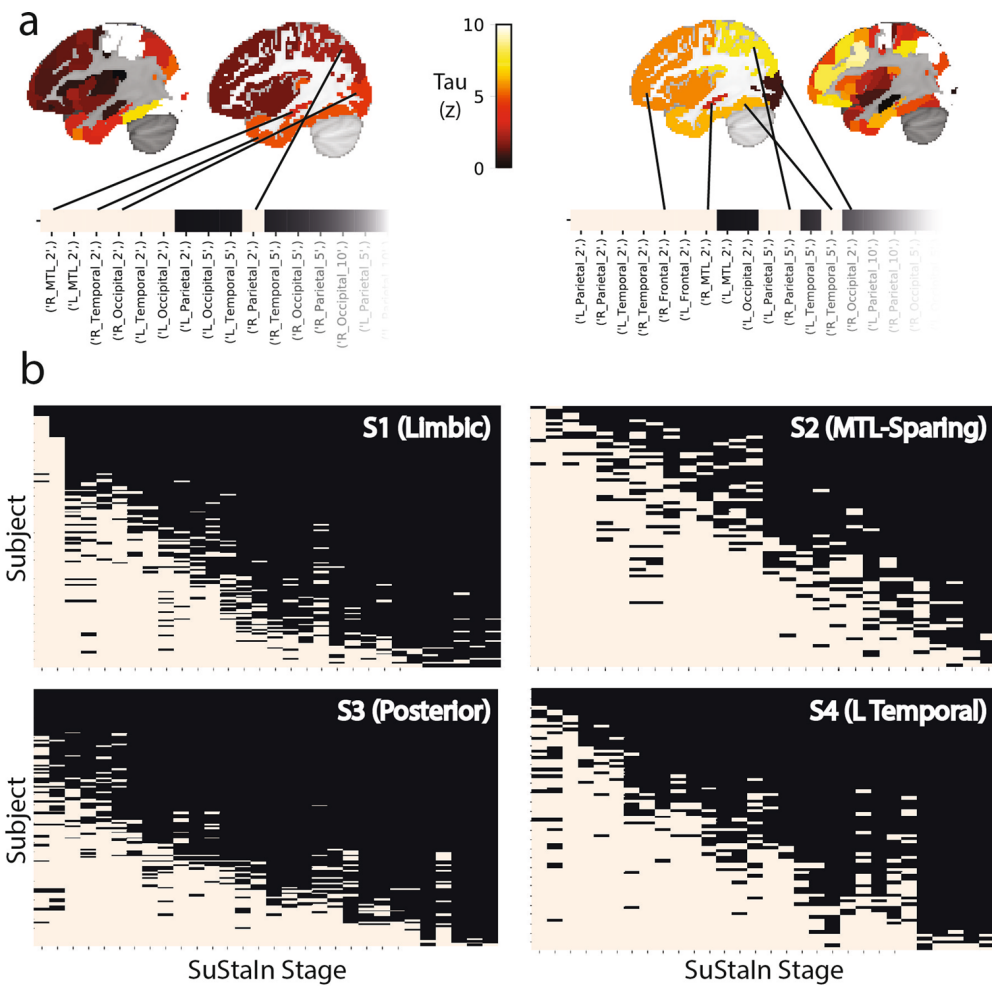
Extended Data Fig. 2 | Details of subtype assignment. Details of subtype assignment. **a**, Several individuals classified as S2 (MTL-Sparing) were found to be tau-negative (that is no significant tau in the entorhinal cortex or precuneus; S2: False). Cortical rendering shows the overall mean tau Z-scores (see Extended Data Fig. 1b) of S2: False individuals. Slightly elevated signal was observed throughout the cortex (but not MTL areas), including in regions where pathological tau is not typically observed until late AD. **b**, Proportion of Ab+ (top) and cognitively impaired (bottom) individuals in S2: False ($n=54$) compared to other S2 individuals (S2: True, $n=79$) and tau-negative individuals (S0, $n=646$). Using, χ^2 -tests with Tukey's posthoc correction, a higher proportion of S2: False and S0 individuals were Ab- (S0 $p[\text{adj}] = 8.5e-13$; S2: F $p[\text{adj}] = 9.7e-08$) and cognitively unimpaired (S0 $p[\text{adj}] = 6.2e-68$; S2: F $p[\text{adj}] = 2.0e-10$) than S2: True individuals, but did not differ significantly from one another (Ab $p[\text{adj}] = 0.94$; cog $p[\text{adj}] = 0.07$). **c**, Using two-sided ANOVAs with Tukey's posthoc correction, S0 and S2: False individuals were older (S0 $p[\text{adj}] = 0.001$; S2: F $p[\text{adj}] = 0.024$) and had higher MMSE scores (S0 $p[\text{adj}] = 0.001$; S2: F $p[\text{adj}] = 0.001$) than S2: True individuals, but did not differ from one another (Age $p[\text{adj}] = 0.48$; MMSE $p[\text{adj}] = 0.21$). **d**, SuStAIn stage of all individuals stratified by subtype, with the poorly fitting subjects (those that had <0.5 probability of falling into any subtype) shown separately. All but one poorly fit subject exhibited very low SuStAIn stages. **e**, Probability of maximum likelihood subtype is low at early SuStAIn stage and quickly increases with increasing SuStAIn stage. **f**, Distribution of clinical diagnoses across SuStAIn stages. **g**, Distribution of clinical diagnoses across subtypes (same colors as in **f**). **h**, Distribution of maximum-likelihood subtype probabilities for each clinical diagnosis. **i**, Distribution of PCA and IvPPA subjects from the UCSF sample into each subtype. For boxplots in **c,e,h**, center line = median, box = inner quartiles, whiskers = extent of data distribution except * = outliers.



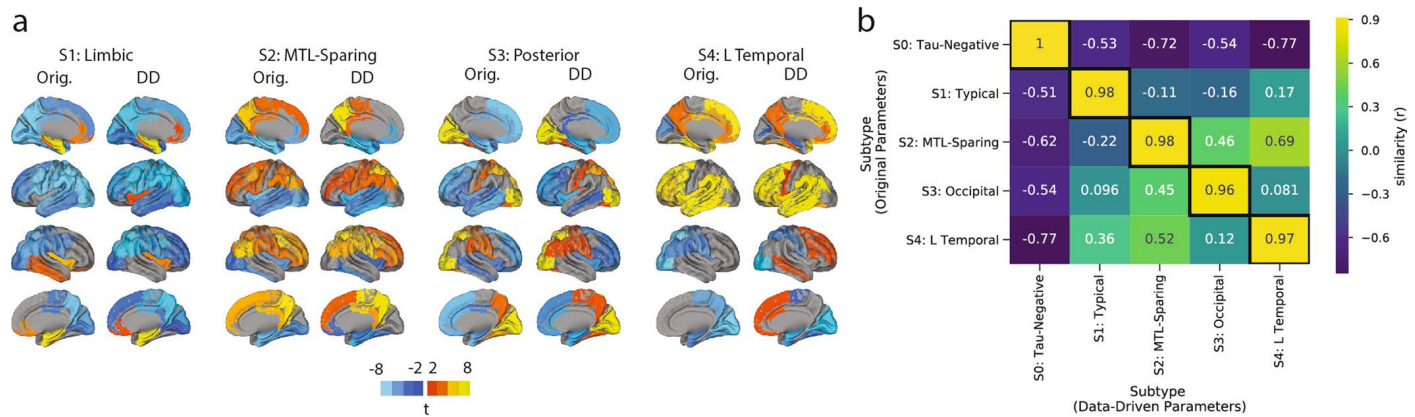
Extended Data Fig. 3 | Regional comparisons. Regional comparisons. Comparison of the mean tau-PET signal (tau-Z) across all ROIs, after adjustment for total cortical tau. A value of 0 represents regional tau Z-score proportionate to the average cortical tau Z-score in that subtype. The left panel represents left hemisphere, the right panel represents right hemisphere. Values represent means \pm SEM.



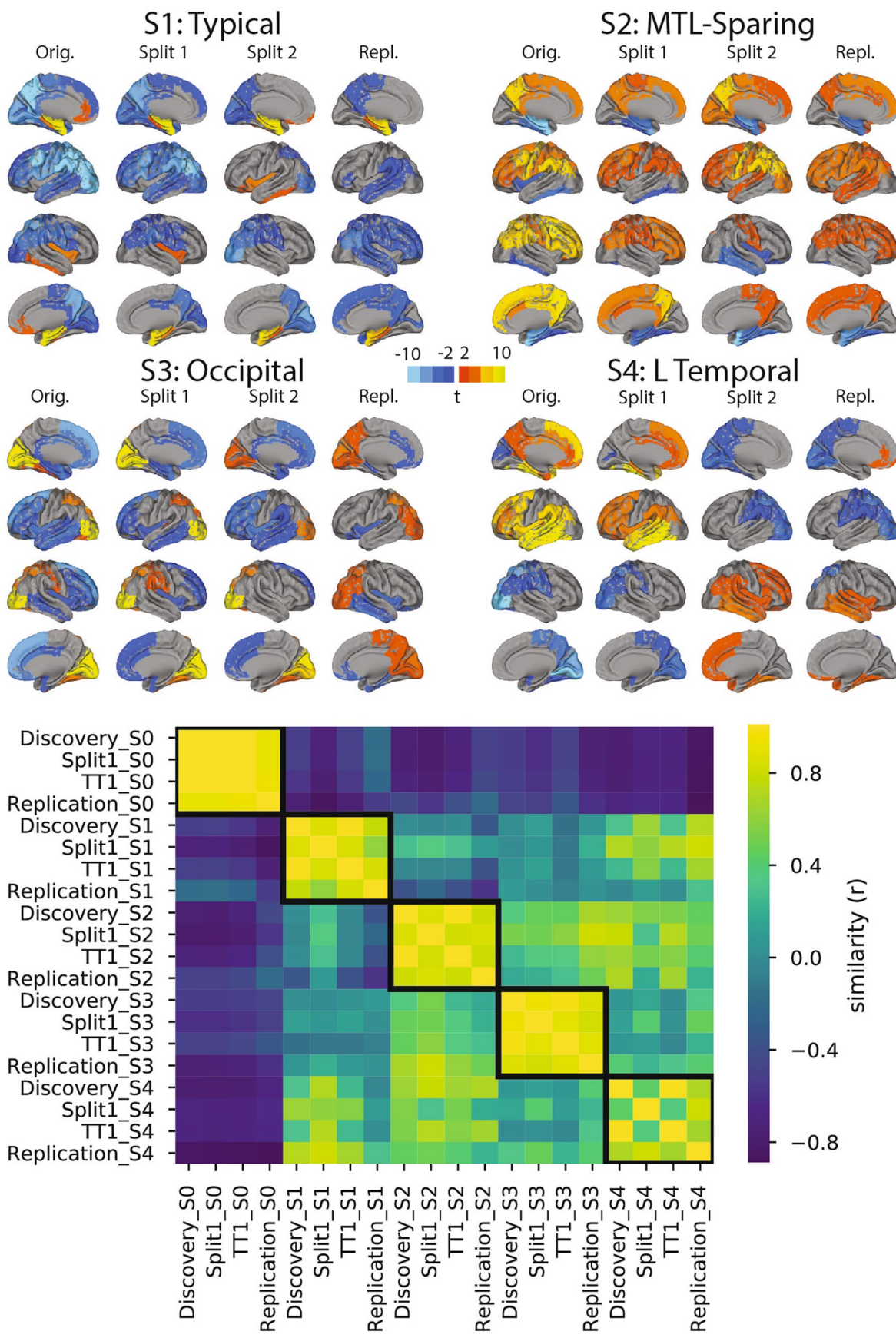
Extended Data Fig. 4 | Subtypes observable across all contributing cohorts. Subtypes observable across all contributing cohorts. The top panel shows the proportions of each subtype (plus S0) within each of the cohorts. All cohorts included individuals from each subtype. The bottom shows the mean tau Z image of each subtypes in a given cohort. Variation can be observed across cohorts, particularly regarding phenotypic severity, but subtype patterns are fairly consistent.



Extended Data Fig. 5 | Individual fit to stereotypical subtype progression. Individual fit to stereotypical subtype progression. **a**) Progression plots are created for each subtyped individual based on their progression through events specific to their subtype. The outer images show regional tau z scores (see Extended Data Fig. 1) for an S2 (left) and S3 (right) individual. This data is summarized in lobar ROI z-scores (inner images). In progression plots under the images, each box represents a biomarker event, SuStain stage. A SuStain stage represents tau reaching a given severity (Z) score at a given region (see Extended Data Fig. 1). Filled (boxes indicate an individual fulfills the criteria for that SuStain stage. An empty (black) box indicates an individual does not. Note that each subtype has a different event order. **b**) A stepwise progression plot is shown for each subtype. Each row represents an individual, and each column represents SuStain stage. A perfect fit would be represented by an individual (row) having every box filled before a given stage, and no boxes filled after. y-axes (subjects) are sorted from the least (top) to most (bottom) stages fulfilled. Across the population, this should be represented as a stepwise progression. Each subtype demonstrates a stepwise progression indicating good general fit. The average subject fit imperfection was 2.1 boxes.

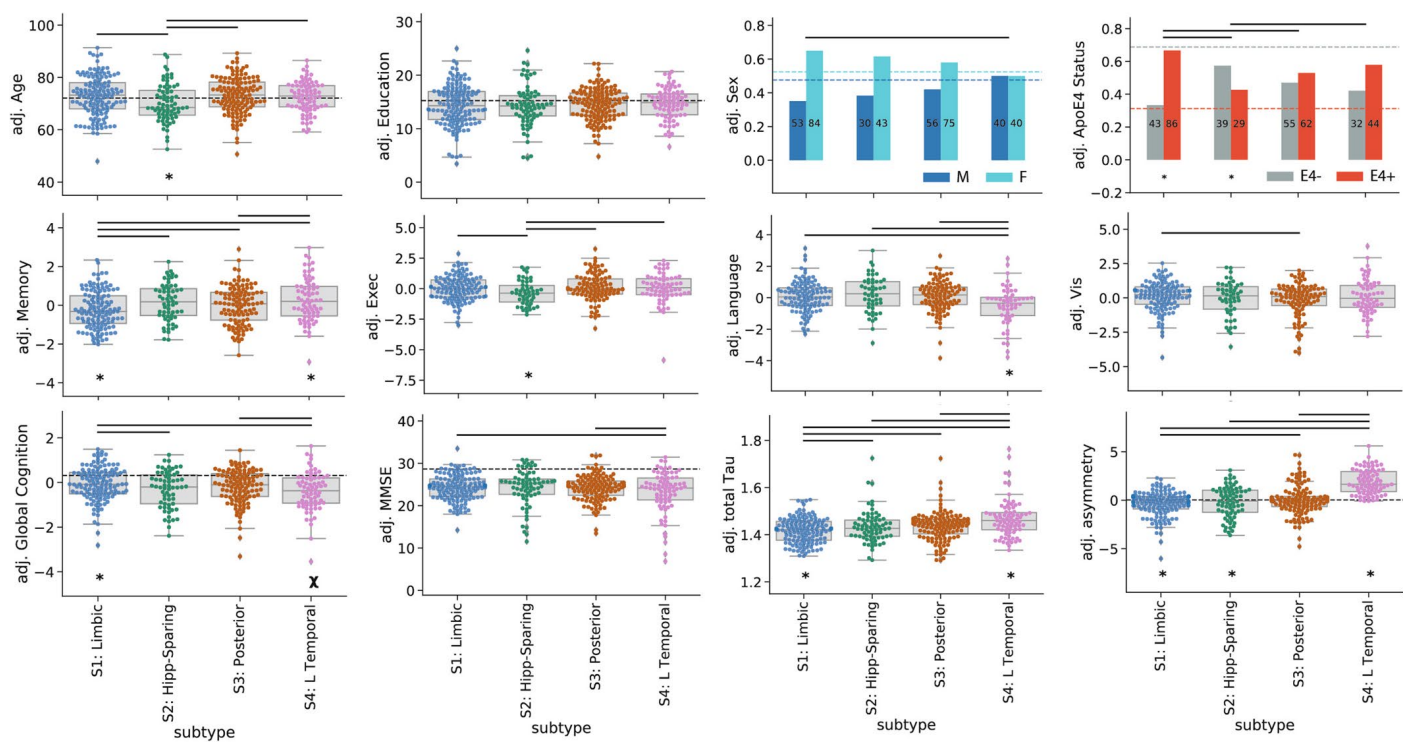


Extended Data Fig. 6 | Replication using different initial parameters. Replication using different initial parameters. SuStain creates nearly identical subtypes when initialized with different parameters (Supplementary Table 5) Methods: Replication Analysis). SuStain was rerun allowing a data-driven methodology to determine the number and value of z-score waypoints for each ROI. **a**) Qualitative contrasts of each subtype as defined using the original (Orig) parameters and the new data-driven (DD) parameters, where maps show regions significantly different between one subtype and all others (excluding S0) within the cohort (after FDR correction). **b**) Confusion matrix comparing subtypes identified in the original (orig) sample (y-axis), and subtypes separately identified in the data-driven parameter replication sample (x-axis). Values represent spatial correlation between average regional tau for each subtype. Values along the diagonal indicates similarity between the same subtype across both parameter sets.

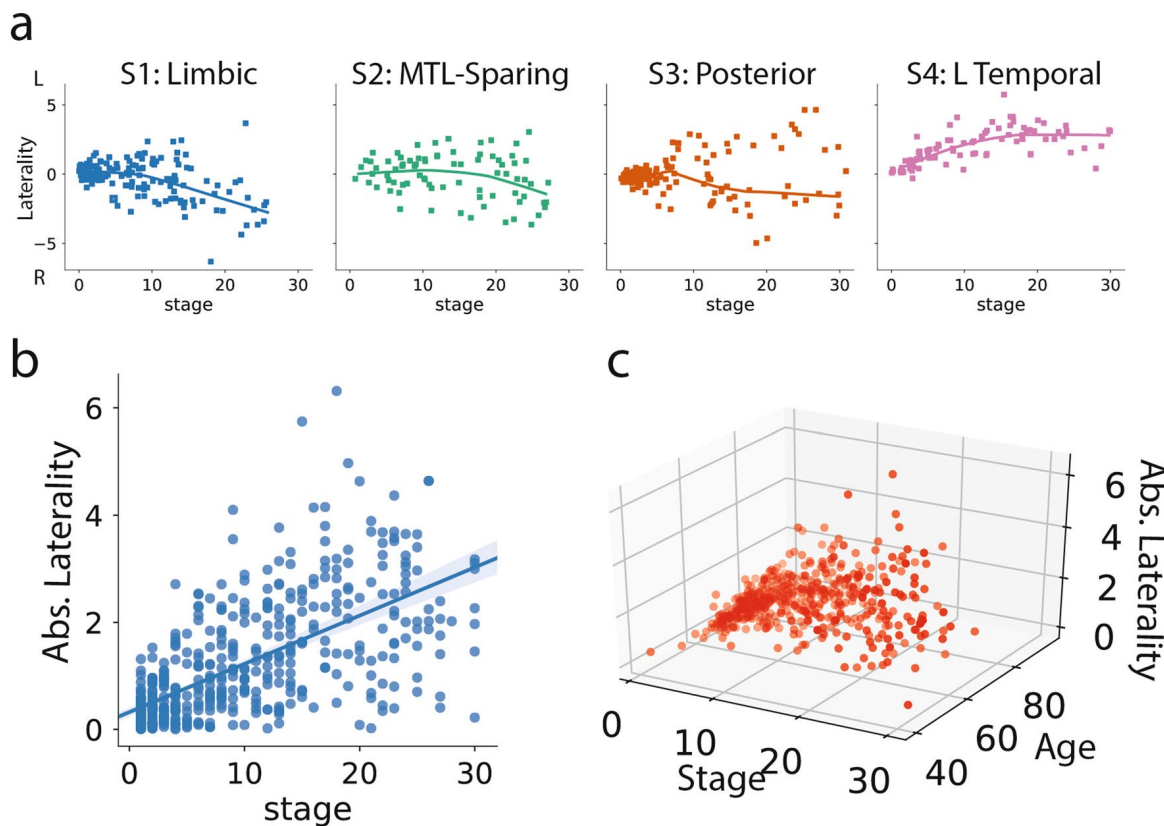


Extended Data Fig. 7 | See next page for caption.

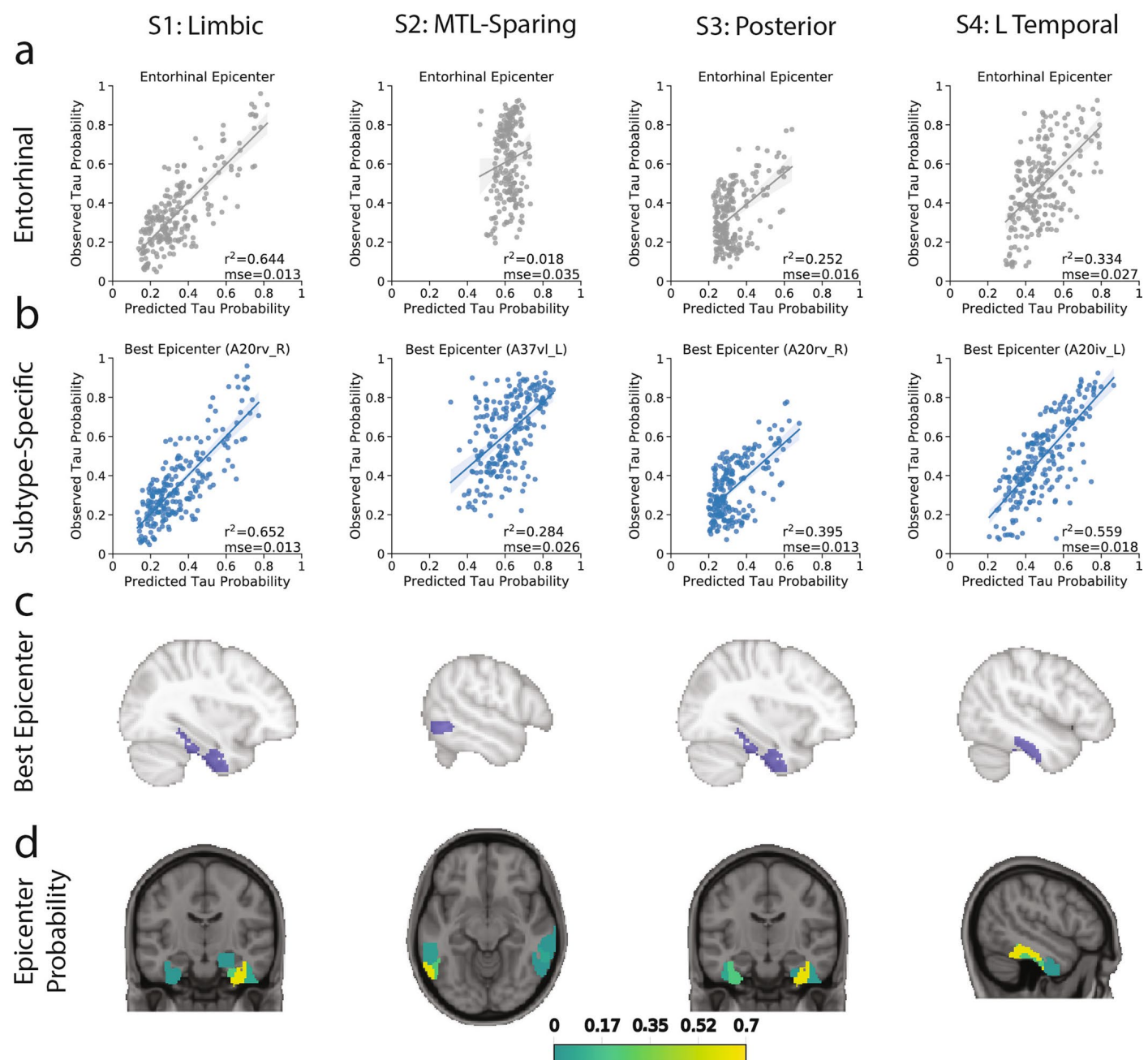
Extended Data Fig. 7 | Stability of subtypes across train-test split and replication datasets. Stability of subtypes across train-test split and replication datasets. (Top) Cortical renders showing, for each subtype across each dataset, regions with significantly different tau-PET signal compared to other within-dataset subtypes after FDR correction. Hot regions show greater tau-PET signal, whereas cooler regions show lower signal. Remarkable similarity can be observed across subtypes, except S4, where lateralization switches from left to right. (Bottom) A heatmap showing similarity (spatial correlation) between subtypes across all four datasets. The diagonal represents identity, whereas outlined boxes represent comparisons of the same subtype across datasets.



Extended Data Fig. 8 | Subtypes present with differing clinical profiles. Subtypes present with differing clinical profiles. For all plots, a * below a box indicates the subtype is significantly different (corrected $p < 0.05$) from other subtypes combined (one vs. all), while a χ represents a trend ($p < 0.1$). Thick horizontal lines above boxes indicate significant ($p < 0.05$) differences between two subtypes (one vs one). Dashed horizontal lines represent the mean of the SO group (controlling for covariates), where relevant. All statistics are adjusted for demographics, disease status, cohort and SuStain stage. For boxplots, the center line=median, box=inner quartiles, whiskers=extent of data distribution except *=outliers.



Extended Data Fig. 9 | Lateralization across disease progression as measured with SuStain stage. Lateralization across disease progression as measured with SuStain stage. **a**, Tau lateralization was measured as the mean left to right ratio of scores for all ten tau features. Higher positive numbers represent greater left hemisphere tau lateralization, whereas lower negative numbers represent greater right hemisphere lateralization. The progression of laterality over SuStain stage was visualized for each subtype. Lateralization generally increased with increasing SuStain stage. In some subtypes (particularly S2 and S3), strong lateralization was seen in both hemispheres later stages. **b**, The absolute (that is agnostic to hemisphere) lateralization was visualized against SuStain stage, indicating general increase in lateralization with more severe tau expression. **c**, A three-way relationship between age, SuStain stage and absolute lateralization is visualized, indicating these relationships covary but are independent of one another. For b, confidence interval represents 95% around line-of-best-fit across 1000 bootstrap samples.



Extended Data Fig. 10 | Replication of subtype-specific epidemic spreading model. Replication of subtype-specific epidemic spreading model. We repeated analyses from Fig. 4, this time using functional connectivity from a sample of elderly healthy and MCI individuals, over a higher-resolution cortical atlas, as the connectome input to the model. The ESM was fit separately for each subtype; once using an entorhinal cortex epicenter (**a**, gray), and once with a subtype-specific best-fitting epicenter (**b**, blue). For each plot, each dot represents a region. The x-axis represents the mean simulated tau-positive probabilities across the population, while the y-axis represents mean observed tau-positive probability. Each column represents a subtype. Confidence interval represents 95% CI around line-of-best-fit across 1000 bootstrap samples **c**) Visualization of the best-fitting epicenter selected by the model. **d**) For each subtype, the probability that each region's best fitting epicenter for that subtype, based on bootstrap resampling (1000 samples).

Reporting Summary

Nature Research wishes to improve the reproducibility of the work that we publish. This form provides structure for consistency and transparency in reporting. For further information on Nature Research policies, see our [Editorial Policies](#) and the [Editorial Policy Checklist](#).

Statistics

For all statistical analyses, confirm that the following items are present in the figure legend, table legend, main text, or Methods section.

n/a Confirmed

- The exact sample size (n) for each experimental group/condition, given as a discrete number and unit of measurement
- A statement on whether measurements were taken from distinct samples or whether the same sample was measured repeatedly
- The statistical test(s) used AND whether they are one- or two-sided
 - Only common tests should be described solely by name; describe more complex techniques in the Methods section.*
- A description of all covariates tested
- A description of any assumptions or corrections, such as tests of normality and adjustment for multiple comparisons
- A full description of the statistical parameters including central tendency (e.g. means) or other basic estimates (e.g. regression coefficient) AND variation (e.g. standard deviation) or associated estimates of uncertainty (e.g. confidence intervals)
- For null hypothesis testing, the test statistic (e.g. F , t , r) with confidence intervals, effect sizes, degrees of freedom and P value noted
 - Give P values as exact values whenever suitable.*
- For Bayesian analysis, information on the choice of priors and Markov chain Monte Carlo settings
- For hierarchical and complex designs, identification of the appropriate level for tests and full reporting of outcomes
- Estimates of effect sizes (e.g. Cohen's d , Pearson's r), indicating how they were calculated

Our web collection on [statistics for biologists](#) contains articles on many of the points above.

Software and code

Policy information about [availability of computer code](#)

Data collection

A custom pipeline was used to preprocess the PET imaging data. Each image underwent motion correction using AFNI's 3dvolreg, and individual PET volumes were averaged within-subject. Each subject's mean PET image next underwent rigid coregistration to its respective skull-stripped native T1 image, and images were intensity normalized using an inferior cerebellar gray reference region, resulting in standardized update value ratio images. T1 images were processed using Freesurfer v6.0, resulting in native space parcellations of each subject's brain using the Desikan-Killiany atlas. These parcellations were used to extract mean SUVR values within different regions of interest for each subject in native space.

Data analysis

Two central analytic modeling algorithms were used in this manuscript. pySuStIn has been described previously (Young et al., 2018 *Nature Communications*) and is available on GitHub (<https://github.com/ucl-pond/pySuStIn>). The Epidemic Spreading Model (ESM) has also been described previously (Iturria-Medina et al., 2014 *PLoS Comp Biol*), and software for user-friendly implementation can be found at <https://www.neuropm-lab.com/>. All other analyses were conducted using Python version 3.7.3, mostly using the following libraries: numpy, pandas, scipy, scikit-learn, statsmodels, matplotlib, seaborn

For manuscripts utilizing custom algorithms or software that are central to the research but not yet described in published literature, software must be made available to editors and reviewers. We strongly encourage code deposition in a community repository (e.g. GitHub). See the Nature Research [guidelines for submitting code & software](#) for further information.

Data

Policy information about [availability of data](#)

All manuscripts must include a [data availability statement](#). This statement should provide the following information, where applicable:

- Accession codes, unique identifiers, or web links for publicly available datasets
- A list of figures that have associated raw data
- A description of any restrictions on data availability

Tau-PET data contributing to this study was sourced from six different cohorts. One of them, ADNI, is a public-access dataset and can be obtained through an application at <http://adni.loni.usc.edu/>. Data from the other datasets are not publicly available for download, but access requests can be made to the respective study Investigators: BioFINDER 1,2 -- Oskar Hansson; UCSF Memory and Aging Center -- Gil D Rabinovici; Gangnam Severence Hospital, Seoul -- Chul Hyoungh Lyoo; AVID Radiopharmaceuticals -- Michael J Pontecorvo, Michael D Devous. Additionally, CMU60 DTI data used to create template DTI connectomes are publicly available, and can be accessed at <https://www.cmu.edu/dietrich/psychology/cognitiveaxon/data.html>

Field-specific reporting

Please select the one below that is the best fit for your research. If you are not sure, read the appropriate sections before making your selection.

Life sciences Behavioural & social sciences Ecological, evolutionary & environmental sciences

For a reference copy of the document with all sections, see nature.com/documents/nr-reporting-summary-flat.pdf

Life sciences study design

All studies must disclose on these points even when the disclosure is negative.

Sample size

Because comprehensive effect size/power calculations have not been comprehensively studied for SuStain, some arbitrary choices were necessary in deciding *a priori* an appropriate sample size. A cardinal recommendation in statistics suggests a minimum of 10 observations (subjects) per variable (feature) (Harrell et al., 1984, Stat Med), and more modern assessments support this recommendation at least in linear, logistic and cox models (Vittinghoff & McCulloch 2007 Am J Epidemiol; Austin & Steyerberg 2015 J Clin Epidemiol; Austin, Allignol & Fine 2017, J Clin Epidemiol). Using this arbitrary rule of at least 10 subjects per feature, since our implementation used 30 features, we anticipated needing 300 subjects. While we initially analyzed 1143 subjects, we anticipated from previous work (Vogel et al., 2020 Nat Comms) that only 40–60% would actually exhibit measurable abnormal tau pathology. For this reason, it was important for us to analyze data from at least 750 subjects, and ideally greater than 1000. We were able to accomplish this goal.

Data exclusions

We excluded individuals with a diagnosis of MCI or any kind of dementia that did not *also* have imaging or CSF evidence of beta-amyloid pathology. Such individuals likely have dementia due to a cause other than Alzheimer's disease. Such cases can at times exhibit unusual tau-PET scans, including diffuse, slightly elevated binding or focal binding in affected regions (e.g. semantic dementia). We feared these cases may interfere with our goal, which was to characterize trajectories of tau spread in AD. It should also be noted that the SuStain algorithm will automatically exclude individuals who do not demonstrate any abnormal events -- in this case, individuals you do not demonstrate abnormal tau-PET signal in the brain.

Replication

We reran the SuStain algorithm completely from scratch in a separate cohort (BioFINDER II), which assessed tau with a different tau-PET radiotracer (RO948). Three out of the four subtypes were unambiguously replicated. The fourth subtype was also quite similar to that of the discovery sample, but featured a hemispheric lateralization opposite to that in the discovery sample. We performed post-hoc analyses and determined this likely to be a consequence of a smaller sample size in the replication set. We also conducted a within-subject longitudinal replication, and we found that 88% of individuals had the same subtype (or went from tau-negative to tau-positive). As a second form of replication, we furthermore refit our model to the original data using completely different input parameters, and this lead to nearly identical results.

Randomization

This is not relevant because we did not conduct a controlled trial. Rather, we combined individuals from several cohorts across the clinical AD spectrum, and applied a data-driven algorithm to derive characteristics from this amassed sample. However, analyses comparing the derived subtypes did covary for age, sex, education, clinical diagnosis, cohort, and disease progression (SuStain stage).

Blinding

Co-authors who performed the data preprocessing were blinded to demographic and clinical characteristics of individuals. Blinding was not relevant for experiments because SuStain is a data-driven technique and received no demographic or clinical data of any kind. Both SuStain and the ESM analyzed were performed only on derivatives of imaging data without any other external information. Therefore, while the researchers were not blinded, the analysis effectively was.

Reporting for specific materials, systems and methods

We require information from authors about some types of materials, experimental systems and methods used in many studies. Here, indicate whether each material, system or method listed is relevant to your study. If you are not sure if a list item applies to your research, read the appropriate section before selecting a response.

Materials & experimental systems

n/a	Involved in the study
<input checked="" type="checkbox"/>	Antibodies
<input checked="" type="checkbox"/>	Eukaryotic cell lines
<input checked="" type="checkbox"/>	Palaeontology and archaeology
<input checked="" type="checkbox"/>	Animals and other organisms
<input type="checkbox"/>	Human research participants
<input checked="" type="checkbox"/>	Clinical data
<input checked="" type="checkbox"/>	Dual use research of concern

Methods

n/a	Involved in the study
<input checked="" type="checkbox"/>	ChIP-seq
<input checked="" type="checkbox"/>	Flow cytometry
<input checked="" type="checkbox"/>	MRI-based neuroimaging

Human research participantsPolicy information about [studies involving human research participants](#)

Population characteristics

This information is provided in detail in Table S1, but for a summary: on average, the participants were 72.1 years old (SD=9). 55% of participants were female and on average, participants had completed some college education. ~60% of subjects were cognitively normal at enrollment, while ~20% had a diagnosis of mild cognitive impairment, and ~20% were diagnosed with AD dementia. 41% of the sample carried at least one APOE4 allele, while 8% carried two APOE4 alleles.

Recruitment

The study sample amassed subjects from six different cohorts. ADNI is a multi-site study that is population-based, but mostly pools from academic centers and excludes for many comorbidities. UCSF is a tertiary memory clinic that recruits many atypical and early-onset forms of AD. BioFINDER 1 and 2 and Gangnam Severance Hospital (Seoul) are also memory clinics, but also recruit from the Swedish and Korean population, respectively. Data from AVID are amassed from several sites relating to different small clinical trials, each with their own recruitment parameters. Overall, the sample is very academic / memory-clinic based, and therefore is enriched for atypical AD cases and more highly educated individuals. This has the disadvantage of being less representative of the population, perhaps over-representing early-onset and aggressive cases, and under-representing older-onset cases with multiple comorbidities. However, such a sample also has the advantage of covering a wide spectrum of AD cases at varying levels of severity including extremes, from many parts of the world, and theoretically with less co-pathology.

Ethics oversight

Informed written consent was provided for all participants or their designated caregiver, and all protocols were approved by each cohort's respective institutional ethical review board. Specifically: All BioFINDER subjects provided written informed consent to participate in the study according to the Declaration of Helsinki; ethical approval was given by the Ethics Committee of Lund University, Lund, Sweden, and all methods were carried out in accordance with the approved guidelines. Approval for PET imaging was obtained from the Swedish Medicines and Products Agency and the local Radiation Safety Committee at Skåne University Hospital, Sweden. For UCSF, the study was approved by the University of California (San Francisco and Berkeley) and Lawrence Berkeley National Laboratory institutional review boards for human research. Data from the AVID sample were collected in compliance with the Declaration of Helsinki and the International Conference on Harmonization guideline on good clinical practice. Data collection for the Gangnam Severance hospital sample was approved by the institutional review board of Gangnam Severance Hospital. Information related to participant consent in ADNI can be found at (ADNI; <http://adni.loni.usc.edu>).

Note that full information on the approval of the study protocol must also be provided in the manuscript.